Chapter 4
Theory and Applications of the Mean Exponential Growth Factor of Nearby Orbits (MEGNO) Method

Pablo M. Cincotta and Claudia M. Giordano

Abstract In this chapter we discuss in a pedagogical way and from the very beginning the *Mean Exponential Growth factor of Nearby Orbits* (MEGNO) method, that has proven, in the last ten years, to be efficient to investigate both regular and chaotic components of phase space of a Hamiltonian system. It is a fast indicator that provides a clear picture of the resonance structure, the location of stable and unstable periodic orbits as well as a measure of hyperbolicity in chaotic domains which coincides with that given by the maximum Lyapunov characteristic exponent but in a shorter evolution time. Applications of the MEGNO to simple discrete and continuous dynamical systems are discussed and an overview of the stability studies present in the literature encompassing quite different dynamical systems is provided.

4.1 Introduction

One of the most challenging aspects of dynamical systems, particularly of those that present a divided phase space, is the understanding of global properties in phase space. Unfortunately, for instance, global instabilities of near-integrable multidimensional Hamiltonian systems are far from being well understood, so in this chapter we should focus on local features, that is, the dynamical behavior in a small domain around a given point of the phase space of the system.

An example of the study of the local dynamics in "every" point of phase space concerns the so-called *chaos detection tools*. This implies the characterization of the dynamical flow around a given initial condition, that is for instance, how two orbits starting very close to each other evolve with time t. A well known result is that for ordered or regular motion, the separation between these two initially

P.M. Cincotta (✉) • C.M. Giordano
Grupo de Caos en Sistemas Hamiltonianos, Facultad de Ciencias Astronómicas y Geofísicas, Universidad Nacional de La Plata and Instituto de Astrofísica de La Plata (CONICET), La Plata, Argentina
e-mail: pmc@fcaglp.unlp.edu.ar; giordano@fcaglp.unlp.edu.ar

Ch. Skokos et al. (eds.), *Chaos Detection and Predictability*, Lecture Notes in Physics 915, DOI 10.1007/978-3-662-48410-4_4

nearby orbits grows linearly with time (or in some particular cases at some power of t); while in those domains where the motion is unstable, chaotic, this separation grows exponentially with t. The rate of this exponential divergence, defined as the limit when $t \to \infty$, is given by the so-called maximum Lyapunov Characteristic Exponent (mLCE). Therefore if we know how to compute efficiently this separation for large times we can obtain a picture of the local dynamics at any given point of phase space. Indeed, in case of regular motion the mLCE vanishes and it has a positive value for chaotic motion (and for unstable periodic orbits).

Another way to characterize the local dynamics is through a spectral analysis. In fact, regular motion proceeds on invariant tori with a constant frequency vector while, when the dynamics is chaotic, the frequencies are no longer local integrals of motion but change with time. Therefore if we managed to develop an accurate technique to measure the frequency of the motion, we could be able to separate the dynamics in regular and chaotic. Moreover, in the regular regime it would be possible to compute the full set of local integrals of motion (that is, the components of the frequency vector).

Since the eighties and mid of the nineties two well known techniques have been available in the literature, an algorithm to compute the mLCE, see for instance [5], and the so called Frequency Map Analysis (FMA [43]). The first one obviously provides the rate of divergence of nearby orbits while the second one is a very precise method to obtain the frequencies of the motion. Both approaches were widely used in many physical and astronomical applications; in particular the FMA was the natural technique to investigate the dynamics of planets and, by means of this tool it was shown that the Solar System as a whole dynamical system is not stable and in fact it is chaotic or marginal unstable [42, 44, 45].

Actually, the mLCE and the FMA (besides the well known Poincaré surface of section for systems with two degrees of freedom), were popular chaos detection tools in dynamical astronomy at those times.

However, computers were not fast enough to deal with large samples of orbits and quite long integration times. For a set of $M \gtrsim 10^6$ orbits, $\sim 12 \times M > 10^7$ nonlinear coupled differential equations should be numerically integrated over long time intervals and with high accuracy in order to get numerical values of the mLCEs close to the expected theoretical ones. For instance, for regular motion the theoretical mLCE $\to 0$ when $t \to \infty$ as $\sim \ln t/t$, so for an evolution time $t \sim 10^4$, a null mLCE numerically means $\sim 10^{-3}$. Thus, it was not possible to distinguish a regular orbit from a chaotic one with a mLCE $\sim 10^{-3}$. Therefore, much larger evolution times would be necessary to discriminate the nature of the motion by the numerical asymptotic value. Thus it becomes clear that 20 years ago, this was a severe restriction to derive precise values of the mLCE.

Since in the end of the nineties several *fast dynamical indicators* appeared in the literature, some of the most popular ones in dynamical astronomy are largely discussed in the present volume. All of them rest on the same theoretical arguments

behind the mLCE, by following the evolution of the flow in a small neighborhood of a given initial condition. Besides, a few new techniques, based on spectral analysis have also been developed which are in fact, slight variations of the FMA. At the end of this chapter we will briefly refer to several of such chaos detection tools.

4.1.1 The MEGNO: Brief History

The MEGNO belongs to the class of the so-called fast dynamical indicators. It is, in fact, a byproduct of a former fast indicator, the *Conditional Entropy of Nearby Orbits*, first proposed in [57] and improved in [10] and [11].

The MEGNO was announced in [11], but neither a description of the method nor a name was provided. In [12], the MEGNO was introduced, but that work was not devoted exclusively to the MEGNO, but to discuss analytical and numerical methods for describing global dynamics in non-axisymmetric galactic potentials in both regimes, regular and chaotic. The MEGNO was addressed there just as an additional and simple tool, and its name (MEGNO) was proposed, following the strong suggestion of one of the reviewers of the paper. The MEGNO was introduced as an efficient way to derive accurately the mLCE. Indeed, in the Introduction of that paper, the authors wrote ... *Alternative techniques were proposed to separate ordered and stochastic motion, to classify orbits in families, to describe the global structure of phase space, but not to get the LCN in shorter times. In Sect. 3 we shall resume this point together with some comparisons with the new technique here presented (MEGNO).... This new tool has proven to be useful for studying global dynamics and succeeds in revealing the hyperbolic structure of phase-space, the source of chaotic motion. The MEGNO provides a measure of chaos that is proportional to the LCN, so that it allows to derive the actual LCN but in realistic physical times...*

It was in [13] that the MEGNO was discussed in detail and a generalization of the original method was presented with applications to both multidimensional Hamiltonian flows and maps.

This chapter is organized as follows. In Sect. 4.2 we address the theory of the MEGNO in a simple fashion, without any intention to enunciate theorems and their concomitant proofs: just several numerical examples would serve to show the expected theoretical behavior of this dynamical indicator. In Sect. 4.3 we present some applications to Hamiltonian flows and symplectic maps. We also yield the results of an exhaustive comparative study of different indicators of chaos in Sect. 4.4. We discuss further applications of the MEGNO that can be found along the literature, from realistic planetary models to bifurcation analysis, in Sect. 4.5. A thorough discussion is provided in the last section.

4.2 The Mean Exponential Growth Factor of Nearby Orbits (MEGNO)

Herein we address the MEGNO's theory following the original presentation given in [13] but in a more pedagogical way.

To that aim, let us consider the phase space state vector

$$\mathbf{x} = (\mathbf{p}, \mathbf{q}) \in B \subset \mathbb{R}^{2N}, \tag{4.1}$$

and introduce the vector field, also defined in B

$$\mathbf{v}(\mathbf{x}) = \left(-\frac{\partial H}{\partial \mathbf{q}}, \frac{\partial H}{\partial \mathbf{p}} \right), \tag{4.2}$$

where $H(\mathbf{p}, \mathbf{q})$ refers to an N-dimensional Hamiltonian, assumed to be autonomous just for the sake of simplicity. The formulation given below however is completely independent of the system being Hamiltonian as well as of the phase space coordinates adopted to express the state vector $\mathbf{x}$. In case of a Hamiltonian system, since the motion in general takes place on a compact energy surface $M_h = \{\mathbf{x} = (\mathbf{p}, \mathbf{q}) \in B : H(\mathbf{p}, \mathbf{q}) = h\}$, thus $\mathbf{x} \in B' \subseteq M_h$, where $\dim(M_h) = 2N - 1$.

Therefore, the equations of motion in B' have the simple form

$$\dot{\mathbf{x}} = \mathbf{v}(\mathbf{x}). \tag{4.3}$$

Let $\varphi(t)$ denote a given solution of the flow (4.3), for a given initial condition $\mathbf{x}_0$,

$$\varphi(t) = \left\{ \mathbf{x}(t; \mathbf{x}_0),\ \mathbf{x}_0 \in B' \right\}. \tag{4.4}$$

For any such an orbit φ the mLCE, $\sigma(\varphi)$, is defined as

$$\sigma(\varphi) = \lim_{t \to \infty} \sigma_1(\varphi(t)), \qquad \sigma_1(\varphi(t)) = \frac{1}{t} \ln \frac{\|\boldsymbol{\delta}(\varphi(t))\|}{\|\boldsymbol{\delta}_0\|}, \tag{4.5}$$

where $\boldsymbol{\delta}(\varphi(t))$ and $\boldsymbol{\delta}_0$ are "infinitesimal displacements" from φ at times t and 0, respectively, and $\|\cdot\|$ denotes the usual Euclidean norm.[1]

In fact, $\boldsymbol{\delta}(\varphi(t))$ is the time evolution of the difference $\varphi'(t) - \varphi(t)$, being $\varphi'(t)$ a nearby orbit to $\varphi(t)$ whose initial condition is $\mathbf{x}'_0 = \mathbf{x}_0 + \boldsymbol{\delta}\mathbf{x}_0$, for $\|\boldsymbol{\delta}\mathbf{x}_0\|$ small enough. The evolution of $\varphi'(t) - \varphi(t)$ after linearizing the flow around $\varphi(t)$ is then computed. Therefore we are evaluating the flow (4.3) and its first variation on a single orbit, instead of computing the evolution of $\varphi'(t)$ and $\varphi(t)$ and performing their difference. This is the very same way in which the algorithm to compute the

[1] Let us note that any other norm could be used all the same.

mLCE was developed. Though it would be possible to integrate the flow to get φ' and φ starting at $\mathbf{x}_0'$ and $\mathbf{x}_0$ respectively, when performing the difference $\varphi'(t)-\varphi(t)$, both in M_h, then after a large but finite time t, the separation between the two orbits would reach, in a chaotic domain, an upper bound $\|\varphi'(t)-\varphi(t)\| \leq d$, where d is the maximum size of the accessible region in M_h. The limiting case when $\|\varphi'(t)-\varphi(t)\| = d$ corresponds to the completely ergodic case, in which any orbit, and also the difference of nearby ones, could fill densely the energy surface M_h.

In any case, the computation of $\varphi'(t)-\varphi(t)$ would provide the right physical insight about the nature of the dynamics in a small neighborhood of $\mathbf{x}_0$, but computationally this is not the best option, since the mLCE measures the divergence of $\delta(t) = \|\varphi'(t)-\varphi(t)\|$ when $t\to\infty$ and $\delta_0 = \|\varphi'(0)-\varphi(0)\| \to 0$.

It is well known that σ provides relevant information about the flow in a small domain around φ. Indeed, recasting (4.5) in the form

$$\sigma(\varphi) = \lim_{t\to\infty}\frac{1}{t}\int_0^t \frac{\dot{\delta}(\varphi(s))}{\delta(\varphi(s))}\mathrm{d}s = \overline{\left(\frac{\dot{\delta}}{\delta}\right)}, \tag{4.6}$$

where $\delta \equiv \|\boldsymbol{\delta}\|$ is the Euclidean norm, $\dot{\delta} \equiv \mathrm{d}\delta/\mathrm{d}t = \dot{\boldsymbol{\delta}}\cdot\boldsymbol{\delta}/\|\boldsymbol{\delta}\|$, and $\overline{(\cdot)}$ denotes time-average, thus it is explicit that the mLCE measures the "mean exponential rate of divergence of nearby orbits".

Thus defined, the so-called tangent vector $\boldsymbol{\delta}$ satisfies the first variational equation of the flow (4.3):

$$\dot{\boldsymbol{\delta}} = \Lambda(\varphi(t))\boldsymbol{\delta}, \tag{4.7}$$

where $\Lambda(\varphi(t)) \equiv \mathrm{D}_{\mathbf{x}}\mathbf{v}(\varphi(t))$ is the Jacobian matrix of the vector field $\mathbf{v}$ evaluated on $\varphi(t)$.

Let us now introduce a slightly different sensitive function on the orbit $\varphi(t)$ which is closely related to the integral in (4.6); the *Mean Exponential Growth factor of Nearby Orbits* (MEGNO), $Y(\varphi(t))$, through

$$Y(\varphi(t)) = \frac{2}{t}\int_0^t \frac{\dot{\delta}(\varphi(s))}{\delta(\varphi(s))}s\mathrm{d}s. \tag{4.8}$$

Recall that in case of an exponential increase of δ, as it occurs for an unstable periodic orbit or a chaotic one, $\delta(\varphi(t)) = \delta_0\exp(\sigma t)$, $\sigma > 0$, $Y(\varphi(t))$ can be considered as a weighted variant of the integral in (4.6). Indeed, instead of the instantaneous rate of growth, σ, we average the logarithm of the growth factor, $\ln(\delta(\varphi(t))/\delta_0) = \sigma t$. Further variants will be considered in Sect. 4.2.2 where the generalization of the MEGNO is addressed.

In what follows we consider some, though quite special, very representative solutions of (4.7) in order to show how $Y(\varphi(t))$ serves to provide clear indication on the character of the motion in each case.

Thus, let us first consider any orbit $\varphi_q(t)$ on a N-dimensional irrational torus in a non-isochronous or nonlinear system. Therefore we can locally define action-angle variables $(\mathbf{I}, \theta)$ such that $\theta(t) = \omega(\mathbf{I})t + \theta_0$, $\mathbf{I} \equiv \mathbf{I}_0$, being $\mathbf{I}_0$ a constant and, for any set of generalized coordinates $(\mathbf{p}, \mathbf{q})$ the solution of (4.3) can be expanded in Fourier series in θ with coefficients that depend on $\mathbf{I}$. Therefore for any such quasiperiodic orbit, φ_q, the solution of (4.7) in generalized coordinates has the form

$$\delta\left(\varphi_q(t)\right) \approx \delta_0\left(1 + w_q(t) + t\left(\lambda_q + u_q(t)\right)\right), \tag{4.9}$$

where $\lambda_q > 0$ is the absolute value of the linear rate of divergence around φ_q, $w_q(t)$ and $u_q(t)$ are oscillating functions (in general quasiperiodic and with zero average) of bounded amplitude, that satisfy $|u_q(t)| \le b_q < \lambda_q$, for some positive constant b_q.[2] The quantity λ_q is a measure of the lack of isochronicity around the orbit and it is related to the absolute value of the maximum eigenvalue of the nonlinearity matrix

$$\frac{\partial \omega_i}{\partial I_j} = \frac{\partial^2 H}{\partial I_i \partial I_j}.$$

Recall that for a linear or quasi-linear system, such as the harmonic oscillator, $\lambda = 0$ for all φ. Indeed, the linear divergence of two nearby quasiperiodic orbits reflects the fact that they move on nearby N-dimensional tori. Since we assume that $\boldsymbol{\omega}$ depends on $\mathbf{I}$, two nearby tori have a small different action vector, say $\mathbf{I}$ and $\mathbf{I} + \delta\mathbf{I}$, and thus $\omega(\mathbf{I} + \delta\mathbf{I}) = \omega(\mathbf{I}) + \delta\omega$. However if $\det\left(\partial\omega_i/\partial I_j\right) = 0$, the system behaves as a linear one and no divergence between two nearby orbits is expected.

From (4.8) and (4.9), keeping in mind that $|u_q|$ is bounded by b_q, it is straightforward to see that $Y(\varphi_q(t))$ oscillates around 2 with bounded amplitude, verifying that

$$|Y\left(\varphi_q(t)\right) - 2| \le 4 \ln \frac{\lambda_q + b_q}{\lambda_q - b_q} \approx 8\,\frac{b_q}{\lambda_q}, \qquad t \to \infty, \tag{4.10}$$

where the last approximation holds if $b_q \ll \lambda_q$. The time evolution of $Y(\varphi_q(t))$ is given by

$$Y\left(\varphi_q(t)\right) \approx 2 - \frac{2\ln(1 + \lambda_q\, t)}{\lambda_q\, t} + O\left(\varphi_q(t)\right), \tag{4.11}$$

where O denotes an oscillating term (with zero average) due to the quasiperiodic character of both $w_q(t)$ and $u_q(t)$. Though

$$\lim_{t\to\infty} Y\left(\varphi_q(t)\right) \tag{4.12}$$

[2] Anyway (4.9) could be empirically derived by numerical means.

does not exist due to the oscillatory term $O\left(\varphi_q(t)\right)$ in (4.11), introducing the time-average

$$\overline{Y}(\varphi_q(t)) \equiv \frac{1}{t}\int_0^t Y(\varphi_q(s))\mathrm{d}s, \tag{4.13}$$

it can readily be seen from (4.10), (4.11) and (4.13) that

$$\overline{Y}\left(\varphi_q\right) \equiv \lim_{t\to\infty} \overline{Y}\left(\varphi_q(t)\right) = 2. \tag{4.14}$$

Therefore, for quasiperiodic motion, $\overline{Y}(\varphi)$ converges to a constant value, which is independent of $\varphi_q(t)$.

The above results still hold in case of a regular orbit $\varphi(t)$ that is not purely stable quasiperiodic. Let us restrict ourselves to 2-dimensional (2D) Hamiltonian systems, though the arguments given below could be straightforwardly extended to higher dimensions and let $\varphi(t)$ be close to a stable periodic orbit, $\varphi_s(t)$. Since $O(\varphi(t))$ in (4.11) involves nearly periodic terms, and both λ and b/λ are small, it follows from (4.10) and (4.11) that $Y(\varphi(t))$ oscillates around 2 with a small amplitude and that $\overline{Y}(\varphi(t))$ converges to 2 slower the smaller is λ. When $\varphi(t) \to \varphi_s(t)$, both $u(t)$, $\lambda \to 0$, and $\overline{Y} \to 0$ as $t \to \infty$. In this limiting case, the oscillations of $Y(\varphi(t))$ about 0 are due to the presence of the term $w(t)$ in (4.9).

Meanwhile, whenever $\varphi(t)$ is close to an unstable periodic orbit, $\varphi_u(t)$, $Y(\varphi(t))$ behaves in a different fashion since in such a case, the motion in any small neighborhood of $\varphi_u(t)$, U, is mainly determined by its associated stable and unstable manifolds. For a sufficiently large motion time, $\varphi(t)$ will pass close to $\varphi_u(t)$ several times. Suppose that between two successive close approaches with $\varphi_u(t)$, $\varphi(t)$ spends a time Δ_1 within U and a time Δ_2 outside U. During the interval Δ_1, $\delta(\varphi(t)) \approx \delta(\varphi_u(t)) \approx \delta_0 \exp(\sigma t)$ with $\sigma > 0$, while, during Δ_2, $\delta(\varphi(t))$ approximately obeys (4.9). The "interaction time" between $\varphi(t)$ and $\varphi_u(t)$, Δ_1, is larger the closer the orbits are to each other. Thus, $Y(\varphi(t))$ should exhibit quasiperiodic oscillations modulated by periodic pulses, of period $\sim \Delta_2$, width $\sim \Delta_1$ and similar amplitude. Analogous considerations apply to $\overline{Y}(\varphi(t))$ but, due to the averaging, the amplitude of the pulses should decrease as $\sim 1/t$. In general, $\overline{Y}(\varphi(t))$ will approach 2 from above and, after a total evolution time t, $\overline{Y}(\varphi(t))$ will be larger the smaller is the distance $\|\varphi(t) - \varphi_u(t)\|$. In the limit, when $\varphi(t) \to \varphi_u(t)$, $\Delta_1 \to t$ and $\delta(\varphi(t))$ grows exponentially with time, so that $\overline{Y}(\varphi(t)) \gg 2$ (see the forthcoming Eq. (4.17) and the so-called "right-stop" criterion discussed in Sect. 4.2.4 that applies for maps).

In case of an irregular orbit, $\varphi_i(t)$, within any chaotic component, the solution of (4.7), besides oscillation terms which are irrelevant in this case, is

$$\delta(\varphi_i(t)) \approx \delta_0 \mathrm{e}^{\sigma_i t}, \tag{4.15}$$

σ_i being the $\varphi_i(t)$'s mLCE. Thus,

$$Y\left(\varphi_i(t)\right) \approx \sigma_i t + \tilde{O}(\varphi_i(t)), \tag{4.16}$$

with $\tilde{O}$ some oscillating term of bounded amplitude which is in general neither periodic nor quasiperiodic, but it has zero average.[3] Note that in a chaotic domain the orbits proceed on a D-dimensional manifold where $N < D < 2N - 1$. In these domains, tori are in general destroyed and the dynamics is said to be hyperbolic since a chaotic orbit could be thought as a slight distortion of an unstable P-periodic orbit with $P \gg 1$.

On averaging (4.16) over a large time interval, we obtain

$$\overline{Y}\left(\varphi_i(t)\right) \approx \frac{\sigma_i}{2}\, t, \quad t \to \infty. \tag{4.17}$$

Therefore, for a chaotic orbit, $Y\left(\varphi_i(t)\right)$ and $\overline{Y}\left(\varphi_i(t)\right)$ grow linearly with time, at a rate equal to the mLCE of the orbit or one half of it, respectively (see below). Only when the phase space has an hyperbolic structure, does Y grow with time. Otherwise, it saturates to a constant value, even in the degenerated cases in which δ grows with some power of t, say n, and therefore $\overline{Y} \to 2n$ as $t \to \infty$.

The MEGNO's temporal evolution allows for being summed up as a single expression valid for any kind of motion, which is not the case for σ_1 or any other chaos indicator. In fact, the asymptotic behavior of $\overline{Y}(\varphi(t))$ may be written in the fashion

$$\overline{Y}(\varphi(t)) \approx a_\varphi t + b_\varphi \tag{4.18}$$

where $a_\varphi = \sigma_\varphi/2$ and $b_\varphi \approx 0$ for chaotic motion, while $a_\varphi = 0$ and $b_\varphi \approx 2$ for stable quasiperiodic motion. Departures from the value $b_\varphi \approx 2$ indicate that φ is close to some periodic orbit, being $b_\varphi \lesssim 2$ and $b_\varphi \gtrsim 2$ for stable or near-unstable periodic orbits, respectively.

Notice that $\hat{\sigma}_1 \equiv Y(\varphi(t))/t$ verifies

$$\hat{\sigma}_1(\varphi_q(t)) \approx \frac{2}{t}, \qquad \hat{\sigma}_1(\varphi_i(t)) \approx \sigma_i, \qquad t \to \infty, \tag{4.19}$$

which show that, for regular motion $\hat{\sigma}_1$ converges to 0 faster than σ_1, which it does as $\ln t/t$, while for chaotic motion both magnitudes approach the positive mLCE at a similar rate.

As it turns out from (4.18) and perhaps the key point of the MEGNO method (but not widespread used) is that, since for chaotic motion $\overline{Y}$ grows linearly with time with a rate $\sigma/2$, a very accurate estimate of the mLCE can be obtained in rather

[3] Since the motion is bounded in phase space, any orbit $\varphi(t)$ should be an oscillating function of time of bounded amplitude, despite if it is regular or chaotic. For unstable or chaotic orbits the main secular growth is given by the exponential term and therefore it is always possible to separate it from a purely oscillating term with zero average.

short times by means of a linear least squares fit on $\overline{Y}(\varphi(t))$. The main feature of this procedure is that it takes advantage of all the dynamical information contained in $\overline{Y}(\varphi(t))$ regarding the whole interval $(t_0, t), t \gg t_0$ and on the fact that $\overline{Y}$ has a smooth behavior. Since for purely quasiperiodic orbits $\overline{Y}(\varphi(t))$ approaches the constant value 2 quite faster than for nearly stable and near-unstable periodic orbits, the mLCE derived from a linear least squares fit of the MEGNO would also yield information on elliptic and hyperbolic points as well.

4.2.1 Comparison of Theoretical and Numerical Results

In order to illustrate the predicted MEGNO's behavior, we regard the well known 2D Hénon–Heiles model [35],

$$H(p_x, p_y, x, y) = \frac{1}{2}(p_x^2 + p_y^2) + \frac{1}{2}(x^2 + y^2) + x^2 y - \frac{y^3}{3}, \tag{4.20}$$

where $x,\ y,\ p_x,\ p_y \in \mathbb{R}$. This Hamiltonian was proposed in the sixties to investigate the existence of the so-called third integral of motion in the Galaxy. We consider the energy level $h = 0.118$. The phase space at this energy level displays at least two main unconnected chaotic domains having different mLCE's as shown by the Poincaré surfaces of section presented in Fig. 4.1 (see, for instance, [11]).

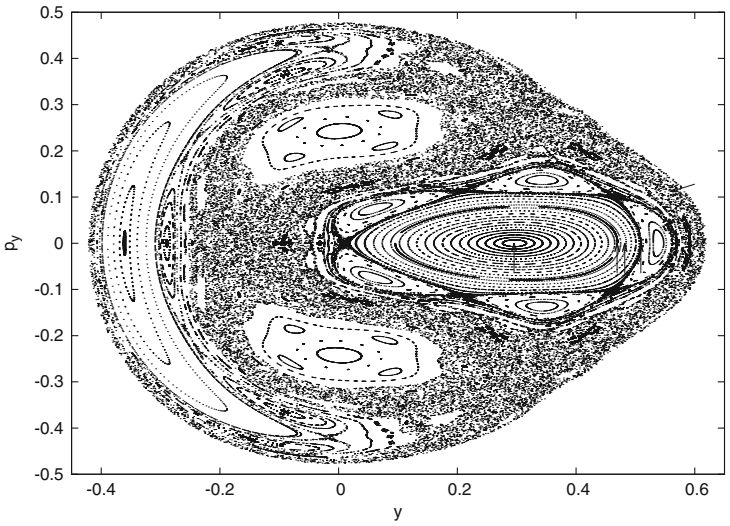

Fig. 4.1 (y, p_y)-Surfaces of section for the Hénon–Heiles Hamiltonian for $h = 0.118, x = 0$, $p_x > 0$. The *arrows* indicate the location of the five initial conditions, *from left to right* (sp), (up), (qp), (c1), (c2). See text

We picked up initial conditions for five representative orbits from the surface $x = 0$: one close to the stable 1-periodic orbit at $(y, p_y) = (0.295456, 0)$ (sp); another one looking like stable quasiperiodic at $(0.483, 0)$ (qp); a third one at $(0.46912, 0)$ also quasiperiodic but close to an unstable 4-periodic orbit (up); and two irregular orbits, one in the stochastic layer surrounding a 5-periodic island chain (or at a $5 : m$ resonance for $m \in \mathbb{Z}_0$) (c1) at $(0.509, 0)$, and the other one lying in a large chaotic sea (c2) at $(0.56, 0.112)$.

We computed Y and $\overline{Y}$ by means of (4.8) and (4.13) respectively; note that the renormalization of $\boldsymbol{\delta}$, if necessary, proceeds naturally from (4.8). Along this work all the numerical integrations were carried out by recourse to a Runge–Kutta 7/8th order integrator (the Dopri8 routine, see [58] and [34]), the accuracy in the conservation of the energy in this case being $\sim 10^{-13}$. The initial tangent vector $\boldsymbol{\delta}$ is chosen at random and with unit norm.[4]

In Fig. 4.2 we show that both Y and $\overline{Y}$ evolve with time as predicted. Indeed, in Fig. 4.2a we observe that, for the stable quasiperiodic orbit (qp), Y oscillates around the value 2 with an amplitude $\lesssim 1$, while $\overline{Y}$ shows a very fast convergence to the actual average (see below).

Figure 4.2b displays the typical behavior of a trajectory close to an unstable periodic orbit. While the (up) orbit is "far away" from the hyperbolic point, both Y and $\overline{Y}$ evolve as in the quasiperiodic case. However, when this quasiperiodic orbit passes close to the unstable one, the mutual interaction causes the oscillations of Y to exhibit a strong modulation, which is damped in $\overline{Y}$ as t increases. Thus, after the first close approach at $t \sim 2000$, $\overline{Y} > 2$ (mainly due to the cumulative effect on the average) but, for t large enough, it asymptotically approaches 2.

Also for the irregular orbits (c1) and (c2) we compute the time-evolution of Y and $\overline{Y}$. The results are given in Fig. 4.2c, where both Y and $2\overline{Y}$ are plotted together to show that, as follows from (4.16) and (4.17), both quantities have the same time-rate. Since the trajectories belong to unconnected chaotic domains, the time-rate (i.e. the mLCE) is different for the two orbits.

In Fig. 4.2d, the temporal evolution of $\overline{Y}$ for all the three regular orbits are compared. For the stable quasiperiodic orbit (qp), $\overline{Y}$ reaches 2 much faster than for the orbit (sp), which is close to a stable periodic one. In fact, $\overline{Y}(\varphi_{sp}) \lesssim 2$ over the full time interval. The time evolution of both, $\overline{Y}(\varphi_{sp})$ and $\overline{Y}(\varphi_{qp})$, fit very well (4.11), on neglecting oscillations and being $\lambda_{sp} < \lambda_{qp}$. We note again just for $\overline{Y}$, that the orbits (qp) and (up) evolve in a rather similar way, as long as the interaction between (up) and its nearby unstable periodic orbit is weak. Therefore, a least squares fit on $\overline{Y}$ could distinguish clearly quasiperiodic orbits from stable and unstable periodic orbits.

In order to show that $\hat{\sigma}_1 \to$ mLCE when $t \to \infty$, in Fig. 4.2e we display its time evolution together with that of σ_1 for three of the orbits, namely, (sp), (c1) and

[4] One should verify that the tangent vector has a non-vanishing component normal to the flow, particularly in the regular component, in order to ensure the linear divergence of nearby orbits (see [16]).

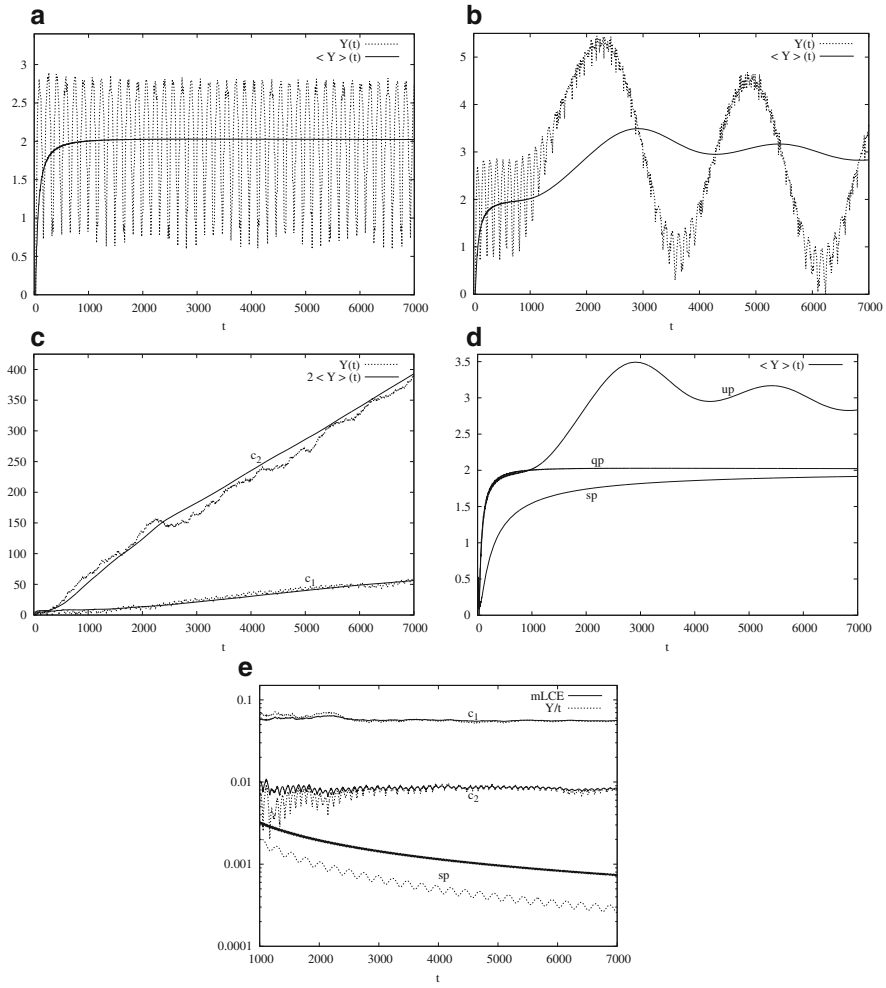

Fig. 4.2 Time evolution of Y and $\overline{Y}$ ($< Y >$ in the figure) for the orbits: (**a**) (qp) stable quasiperiodic; (**b**) (up) quasiperiodic but close to an unstable 4-periodic orbit; (**c**) (c1) and (c2) irregular, embedded in two different chaotic domains. (**d**) $\overline{Y}$ ($< Y >$ in the figure) for three regular orbits: (sp) close to a stable periodic orbit, (qp), and (up); (**e**) time evolution of $\hat{\sigma}_1$ (Y/t in the figure) and the mLCE, σ_1 for (sp), (c1) and (c2) computed using the algorithm given in [5]

(c2). We observe that for the chaotic orbits, both magnitudes converge to the same positive mLCE at the same rate. For the regular orbit (sp) instead, we note that $\hat{\sigma}_1$ decreases faster than σ_1, the expected final values (see (4.19) and discussion below), 0.0013 and 0.00028 respectively, being the latter close to the computed one.

In the case of chaotic motion, both Y and $\overline{Y}$ evolve almost linearly with time over the whole time interval, as shown in Fig. 4.2c. The deviations from the linear trend, for instance in (c2), are presumably caused by stickiness. Indeed, during those

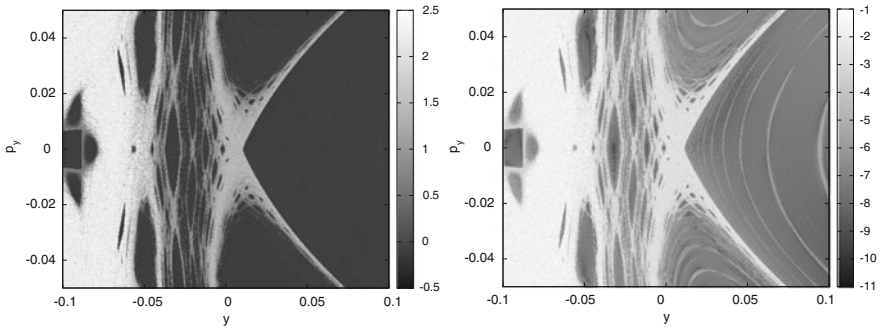

Fig. 4.3 (y, p_y)-Surface of section of the Hénon–Heiles Hamiltonian for $h = 0.118, x = 0, p_x > 0$. The *left panel* corresponds to MEGNO contour plot in logarithmic scale ($\log 2 \approx 0.3$) and in the *right panel* the mLCE, also in logarithmic scale, derived from a linear least squares fit on $\overline{Y}$. See text for details

time intervals, Δt_s, in which Y is almost flat, the orbit remains close to some small stability domain embedded in the chaotic sea. In this particular example, stickiness does not significantly reduce the linear trend but, whenever it is strong, it does influence the mean time-rate of both Y and $\overline{Y}$ and consequently, the derived mLCE. However, the same effect would be present in the numerical computation of the mLCE, since the stickiness phenomena affects the evolution of $\delta(t)$ and therefore if $\delta(t)$ does not increase exponentially within Δt_s, the evolution of $\sigma_1(t)$ would decrease with time as $\sim \ln t/t$ while $t \in \Delta t_s$.

Finally, in Fig. 4.3 we present a small domain of the (y, p_y)-surface of section of the Hénon–Heiles Hamiltonian for $h = 0.118$, $x = 0$, $p_x > 0$ given in Fig. 4.1, the contour plots providing, in logarithmic scale, the MEGNO and the mLCE computed by a least squares fit on the time evolution of $\overline{Y}$ over the time interval (t_0, t) with $t = 10^4$, $t_0 = 2 \times 10^3$. A given $t_0 > 0$ is adopted in order to avoid the initial transient; thus, the least squares fit is performed over the 80 % of the full time interval. From these two plots we observe that the MEGNO provides a clear picture of the dynamics but the accurate value of the mLCE obtained following this alternative procedure furnishes more information than the MEGNO itself. Indeed, both plots show up the very same information in the chaotic domain, however, the MEGNO does not separate clearly the thin unstable domain inside the stability island as the mLCE computed by a least squares fit does. Note that using a simple least squares fit on the time evolution on $\overline{Y}$ over the 80 % of the whole time interval, we reach values of the mLCE for regular motion of the order of 10^{-10} or lower considering motion times $t \sim 10^4$, when the expected lower value of the mLCE by recourse to the classical algorithm would be $\sim 10^{-3}$. This is, in our opinion, one of the main results provided by the MEGNO: its very accurate determination of the positive and null mLCE, for chaotic and regular motion respectively.

Further details on the MEGNO's performance when applied to the study of the dynamics of 2D Hamiltonians, as well as other advantages of deriving the mLCE from a least squares fit on $\overline{Y}$ are given in [12].

4.2.2 Generalization of the MEGNO

Let us generalize the MEGNO by introducing the exponents (m, n) such that

$$Y_{m,n}\left(\varphi(t)\right) = (m+1)\ t^n \int_0^t \frac{\dot{\delta}(\varphi(s))}{\delta(\varphi(s))}\ (s)^m\ \mathrm{d}s, \tag{4.21}$$

now defining

$$\overline{Y}_{m,n}\left(\varphi(t)\right) = \frac{1}{t^{m+n+1}} \int_0^t Y_{m,n}\left(\varphi_q(s)\right)\ \mathrm{d}s, \tag{4.22}$$

and analyze whether any benefit would turn out when taking values for the exponents $(m, n), m \geq 0$ other than the natural choice $(1, -1)$ which yielded (4.8) and (4.13). Note that in the limit when $t \to \infty$, $Y_{0,-1} \to \sigma$ as defined in (4.6).

The time evolution of $Y_{m,n}$ for regular, quasiperiodic motion, is given by

$$\begin{aligned} Y_{m,n}\left(\varphi_q(t)\right) \approx (m+1) &\left(\sum_{k=0}^{m-1} \frac{(-1)^k t^{m+n-k}}{(m-k)\lambda_q^k}\right) \\ &+(m+1)\left((-1)^m \frac{t^n \ln(1+\lambda_q\, t)}{\lambda_q^m}\right) + O\left(\varphi_q(t)\right), \end{aligned} \tag{4.23}$$

which naturally reduces to (4.11) for $(m, n) = (1, -1)$. This expression is obtained by replacing the value of $\delta\left(\varphi_q(t)\right)$ given by (4.9) in (4.21). Notice that for t large enough we get

$$\frac{Y_{m,n}\left(\varphi_q(t)\right)}{t^{m+n}} \approx \frac{(m+1)}{m}, \tag{4.24}$$

so the ratio $Y_{m,n}/t^{m+n}$ saturates to a constant as $t \to \infty$.

Moreover, from both (4.22) and (4.23) it follows that

$$\overline{Y}_{m,n}\left(\varphi_q(t)\right) \approx \frac{(m+1)}{m\,(m+n+1)}, \quad t \to \infty, \tag{4.25}$$

which is also a fixed constant not depending on the orbit.

For an irregular orbit, φ_i, with mLCE σ_i, we have

$$\frac{Y_{m,n}\left(\varphi_i(t)\right)}{t^{m+n}} \approx \sigma_i\ t + \tilde{O}\left(\varphi_i(t)\right), \tag{4.26}$$

while, on considering a sufficiently large time, we obtain

$$\overline{Y}_{m,n}\left(\varphi_i(t)\right) \approx \frac{\sigma_i\ t}{(m+n+2)}. \tag{4.27}$$

For a chaotic orbit then, both $Y_{m,n}/t^{m+n}$ and $\overline{Y}_{m,n}$, thus defined, grow linearly with time, at a rate that is proportional to the mLCE of the orbit.

Therefore, the asymptotic behavior of $\overline{Y}_{m,n}$ can be recast as

$$\overline{Y}_{m,n}\left(\varphi(t)\right) \approx a_\varphi t + b_\varphi, \tag{4.28}$$

where now $a_\varphi = \sigma_i/(m+n+2)$ and $b_\varphi \approx 0$ for irregular, chaotic motion, while $a_\varphi = 0$ and $b_\varphi \approx (m+1)/m(m+n+1)$ for stable, quasiperiodic motion. As it turns out from (4.28), the mLCE can also be recovered by a simple linear least squares fit on $\overline{Y}_{m,n}\left(\varphi(t)\right)$.

Notice that $\hat{\sigma}_{1,m,n} = Y_{m,n}/t^{m+n+1}$ satisfies

$$\hat{\sigma}_{1,m,n}(\varphi_q(t)) \approx \frac{(m+1)}{m\ t}, \qquad \hat{\sigma}_{1,m,n}(\varphi_i(t)) \approx \sigma_i, \qquad t \to \infty, \tag{4.29}$$

so that, for regular motion, $\hat{\sigma}_{1,m,n}$ also converges to 0 faster than $\sigma_1 \sim \ln t/t$, while for chaotic motion, both magnitudes approach the positive mLCE at a similar rate.

An exhaustive comparison of the generalized MEGNO's performance for different exponents (m,n) revealed that, besides the natural choice $(1,-1)$, the values $(2,0)$ serve to distinguish regular from chaotic behavior in a quite efficient manner (see below).

Just for the sake of illustration, let us turn back to the 2D Hénon–Heiles example given in Sect. 4.2.1. For the same three regular orbits labeled as (sp), (qp) and (up), we computed both $Y_{m,n}$ and $\overline{Y}_{m,n}$, by means of (4.21) and (4.22) respectively, for three different choices of (m,n), namely, $(1,-1)$, $(2,0)$ and $(3,1)$.

In Fig. 4.4 we show that for regular motion, $\overline{Y}_{m,n}$ evolves with time as predicted by (4.25). Indeed, the temporal evolution of $\overline{Y}_{m,n}$ for the three regular orbits is seen to tend to the asymptotic values 2, $1/2$ and $4/15$, when the exponents are $(1,-1)$, $(2,0)$ and $(3,1)$, respectively. We note that, for the stable quasiperiodic orbit (qp), $\overline{Y}_{m,n}$ converges to the value given in (4.25), a faster convergence being observed the larger is m. Also for the orbit close to a stable periodic one (sp), does $\overline{Y}_{m,n}$ reach the constant value (4.25) faster as a larger exponent m is considered. Notice however that for $m = 2$ much smaller oscillations around the asymptotic value (4.25) are observed in the case of the trajectory close to an unstable periodic orbit (up). Let us note that the exponent n is dummy in the present discussion.

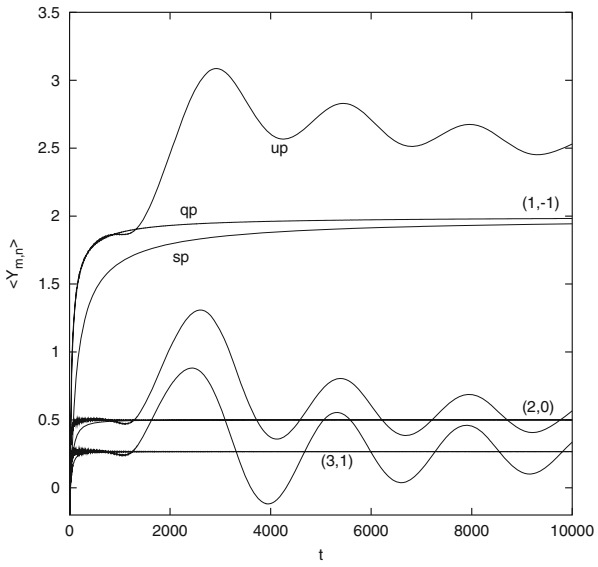

Fig. 4.4 Time evolution of $\overline{Y}_{m,n}$ ($< Y >_{m,n}$ in the plot) for the regular orbits (sp), (qp) and (up) in the Hénon–Heiles model, for different values of the exponents (m, n). Figure taken from [13]

From this comparison we conclude that the choice of exponents $(2, 0)$ allows for clearly separating regular and chaotic regime even in rather short evolution times. Furthermore, if we use as a dynamical indicator the quantity $4\overline{Y}_{2,0}$, we see that for regular orbits it tends to 2, as $\overline{Y}_{1,-1}$ does, while for orbits with exponential instability it tends to $\sigma_i t$. Then, either a linear fit or simply $4\overline{Y}_{2,0}(\varphi_i(t))/t$ provides an estimate of the mLCE. However, the choice $(1, -1)$ for the exponents offers the additional benefit of more clearly identifying stable and unstable periodic motion as well. Anyway, though all the eventual advantages of the generalized MEGNO showed above, the use of the classical MEGNO, $\overline{Y}_{1,-1}$, is widespread. Therefore, we will show the results for $\overline{Y}_{2,0}$ when dealing with discrete applications and discuss below an interesting connection between the classical MEGNO and another well known chaos indicator.

4.2.3 The Connection Between the MEGNO and the FLI

The standard MEGNO, defined adopting the value of the exponents $(1, -1)$, exhibits an intrinsic relation with the classical Fast Lyapunov Indicator (FLI) [53], as we will see in the sequel. For that sake we recall that in [18] the authors define the FLI for a given solution of the flow (4.3), $\varphi(t)$, in terms of the norm of the tangent vector

$\delta \equiv \|\boldsymbol{\delta}\|$ as

$$\mathrm{FLI}(\varphi(t)) = \ln \delta(\varphi(t)), \tag{4.30}$$

expression that has been used to obtain analytical results in both [18] and [33].

Thus, the time average of the FLI in the interval $(0, t)$ is given by

$$\overline{\mathrm{FLI}}(\varphi(t)) = \frac{1}{t}\int_0^t \ln \delta(\varphi(s))ds. \tag{4.31}$$

The MEGNO is twice a time weighted average of the relative divergence of orbits as it can be seen from (4.8). In order to show the relation between the MEGNO and the FLI, let us rewrite (4.8) in the fashion:

$$Y(\varphi(t)) = \frac{2}{t}\int_0^t \frac{d}{ds}\left(\ln \delta(\varphi(s))\right) ds. \tag{4.32}$$

After a simple manipulation we obtain

$$Y(\varphi(t)) = 2\left\{ \ln \delta(\varphi(t)) - \frac{1}{t}\int_0^t \ln \delta(\varphi(s))ds \right\}, \tag{4.33}$$

where the value $\delta(0) = 1$ has been taken. From (4.30), (4.31) and (4.33) we conclude that the MEGNO is twice the difference between the FLI and its time average over the interval $(0, t)$,

$$Y(\varphi(t)) = 2\left\{\mathrm{FLI}(\varphi(t)) - \overline{\mathrm{FLI}}(\varphi(t))\right\}. \tag{4.34}$$

This result serves to understand two facts that have been recently mentioned in the literature. One point is that the MEGNO criterion takes advantage of the dynamical information of the evolution of the tangent vector along the complete orbit, as stated in [70] and [37]. Equation (4.34) tells us exactly in which way it encompasses this information: at every time the MEGNO subtracts from the FLI its average value.

The other point worth discussing, which is explicitly mentioned in [7] and [3], is the reason by which the MEGNO gives account of the degree of chaoticity of an orbit in an absolute scale while the FLI just gives relative values; i.e. in the case of regular orbits the MEGNO tends asymptotically towards a constant value (2), while the FLI behaves logarithmically, not allowing to count with a time independent criterion to establish the threshold that separates chaotic from regular motion.

Just to illustrate this situation let us consider the case of an ideal KAM regular orbit. Therefore the norm of the tangent vectors behaves as (4.9) and besides oscillations $\delta(\varphi_q(t)) \approx 1 + \lambda t$ ($\lambda > 0$ and $\delta_0 = 1$). In this case it is

$$\mathrm{FLI}(\varphi_q(t)) \approx \ln(1 + \lambda t) \tag{4.35}$$

and

$$\overline{\mathrm{FLI}}((\varphi_q(t))) \approx \ln(1+\lambda t) + \frac{\ln(1+\lambda t)}{\lambda t} - 1. \tag{4.36}$$

Therefore, on regarding (4.34) there results

$$Y(\varphi_q(t)) = 2\left\{1 - \frac{\ln(1+\lambda t)}{\lambda t}\right\}, \tag{4.37}$$

and we rediscover the already mentioned asymptotic limit of the MEGNO for regular orbits.

On the other hand, in the case of an ideal chaotic orbit, with $\delta(\varphi_i(t)) \approx \mathrm{e}^{\sigma t}$ (being σ the mLCE), the MEGNO-FLI relation allows to prove that both indicators behave similarly, that is linearly with time with a slope equal to σ.

In order to show the MEGNO-FLI relation we consider again the Hénon–Heiles model for the same energy level, $h = 0.118$, and two orbits one quasiperiodic at $y = 0.2, p_y = 0$ inside the largest island, and a chaotic one at $y = -0.18, p_y = 0$ in the chaotic sea. Just to eliminate oscillations, we compute $\overline{Y}(\varphi(t))$ and the average of $\left\{\mathrm{FLI}(\varphi(t)) - \overline{\mathrm{FLI}}(\varphi(t))\right\}$ for these two orbits. The results presented in Fig. 4.5 show an excellent agreement between both magnitudes.

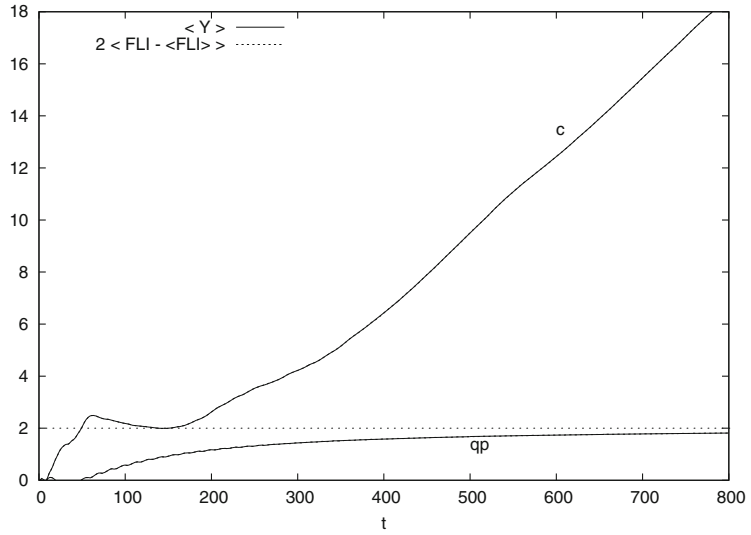

Fig. 4.5 Illustration of the relation (4.34)—in average—for a quasiperiodic orbit (qp) and a chaotic (c) one for the Hénon–Heiles system at $h = 0.118$. Note that both curves are indistinguishable

Therefore in view of the close relation between the MEGNO and the FLI, any improvement concerning the FLI, as for instance the alternative version of the FLI, the so-called Orthogonal Fast Lyapunov Indicator (OFLI)—see [16] and the corresponding chapter in this volume—, applies naturally to improve the MEGNO itself.

4.2.4 The MEGNO for Maps

In this subsection we briefly show how the MEGNO should be implemented to discrete dynamical systems. For dealing with maps, this numerical tool is defined essentially as before, but summing over the iterates of the map instead of integrating with respect to t, and taking the differential map in place of the first variational equations.

For a given initial point P_0, iterates under a given map T are computed yielding points $P_k = T^k(P_0)$. An initial random and unitary tangent vector $\mathbf{v}_0$, is transported under the differential map DT, to obtain vectors $\mathbf{v}_k = DT^k(P_0)\mathbf{v}_0$. Then, after N iterates, the (generalized) MEGNO is computed by means of

$$Y_{m,n}(N) = (m+1)\, N^n \sum_{k=1}^{N} \ln\left(\frac{\|\mathbf{v}_k\|}{\|\mathbf{v}_{k-1}\|}\right) k^m, \tag{4.38}$$

and

$$\overline{Y}_{m,n}(N) = \frac{1}{N^{m+n+1}} \sum_{k=1}^{N} Y_{m,n}(k)\,. \tag{4.39}$$

We have considered different values for the exponents m and n. Again, it turned out that the larger m, the faster $\overline{Y}_{m,n}$ converges to a constant value for regular motion, but, for m rather large, small oscillations show up. However, the bumpy late evolution of $\overline{Y}_{m,n}$ (which is also present in the continuous case, as Fig. 4.4 shows, in the case of (up) orbits) is diminished if the iteration is stopped when the distance between the initial and final points is minimum ("right-stop" condition). On returning close to the initial point, the effect of the periodic or quasiperiodic oscillations added to a regular behavior is minimized. This sort of refinement in regards to the stop time in the case of maps has proven rather efficient in smoothing such oscillations.

The choice $(2, 0)$ for the exponents, together with the "right-stop" condition, have shown to provide a fairly good fast dynamical indicator for maps. A minor additional modification is also convenient with the choice $(m, n) = (2, 0)$. Let us define the parameter

$$\hat{Y}_{2,0}(N) = \frac{4\overline{Y}_{2,0}(N) - 2}{N}, \tag{4.40}$$

which when $N \to \infty$, $\hat{Y}_{2,0} \to 0^-$ for orbits lying on tori, while $\hat{Y}_{2,0} \to \sigma_i$ in the case of chaotic orbits that lie in a higher dimensional domain. So, negative values (close to 0) of $\hat{Y}_{2,0}(N)$ arise for regular orbits (provided N is taken not too small), while small positive values would identify mild chaos.

4.3 Applications

4.3.1 A System of Continuous Time: The Arnold Model

Let us consider the well known classical Arnold Hamiltonian [1], which is the paradigmatic model that leads to the so-called (and perhaps controversial) Arnold diffusion. We will address this simple but very representative nonlinear model because, in our opinion, it has not been discussed in a plain manner for non-mathematical readers yet. In fact, though Sect. 7 in [8] is devoted to present Arnold diffusion in an heuristic way by recourse to this model, unfortunately that section of the outstanding review by B. Chirikov seems not to be widespread in the nonlinear community. The Arnold model is also well discussed in the lectures of Giorgilli [24], though in a more mathematical fashion.

The Arnold Hamiltonian has the form

$$H(I_1, I_2, \theta_1, \theta_2, t; \varepsilon, \mu) = \frac{1}{2}(I_1^2 + I_2^2) + \varepsilon(\cos\theta_1 - 1)(1 + \mu B(\theta_2, t))$$
$$B(\theta_2, t) = \sin\theta_2 \; + \; \cos t, \tag{4.41}$$

with $I_1, I_2 \in \mathbb{R}$, $\theta_1, \theta_2, t \in \mathbb{S}^1$; where μ should be exponentially small with respect to ε, so that $\varepsilon\mu \ll \varepsilon \ll 1$ (just in Arnold formulation, however see below).

For $\varepsilon = 0$ we have two integrals of motion, namely I_1 and I_2 which determine the invariant tori supporting the quasiperiodic motion with frequencies $\omega_1 = I_1$, $\omega_2 = I_2$. Therefore we have a very simple dynamical system consisting of two uncoupled free rotators, so that, $\theta_1(t) = I_1 t + \theta_1^0$, $\theta_2(t) = I_2 t + \theta_2^0$.

For $\varepsilon \neq 0$, $\mu = 0$ we still have two integrals,

$$H_1(I_1, \theta_1; \varepsilon) = \frac{1}{2}I_1^2 + \varepsilon(\cos\theta_1 - 1), \quad I_2, \tag{4.42}$$

and the unperturbed Hamiltonian could be written as

$$H_0(I_1, I_2, \theta_1; \varepsilon) = H_1(I_1, \theta_1; \varepsilon) + \frac{1}{2}I_2^2. \tag{4.43}$$

Notice that H_1 is the pendulum model for the resonance $\omega_1 = 0$; $H_1 \equiv h_1 = -2\varepsilon$ corresponds to the exact resonance or stable equilibrium point at $(I_1, \theta_1) = (0, \pi)$

while $h_1 = 0$ to the *separatrix* and thus $(I_1, \theta_1) = (0, 0)$ is the unstable point or *whiskered torus*.[5]

The associated frequencies are now $\omega_1 = \omega_p(h_1, \varepsilon)$, $\omega_2 = I_2$, where $\omega_p(h_1, \varepsilon)$ is the pendulum frequency,

$$\begin{aligned} \omega_p(h_1, \varepsilon) &= \frac{\pi \omega_0(\varepsilon)}{2K\left(k_{h_1}\right)}, \qquad -2\varepsilon \le h_1 < 0, \\ \omega_p(h_1, \varepsilon) &= \frac{\pi \omega_r(h_1, \varepsilon)}{2K\left(k_{h_1}^{-1}\right)}, \qquad h_1 > 0; \end{aligned} \tag{4.44}$$

where $k_{h_1}^2 = (h_1 + 2\varepsilon)/2\varepsilon$, $\omega_0(\varepsilon) \equiv \sqrt{\varepsilon}$ is the small oscillation frequency, $\omega_r(h_1, \varepsilon) = \omega_0(\varepsilon) k_{h_1}$ is the half-rotation frequency and $K(\kappa)$ is the complete elliptical integral of the first kind. For rotations, the second in (4.44) provides the half-rotation frequency, in order to avoid the jump of a factor 2 between the frequency at both sides of the separatrix. Therefore in the oscillation regime $\omega_p(h_1, \varepsilon) \le \omega_0(\varepsilon)$ and close to the separatrix for both oscillations and rotations, $\omega_p(|h_1| \ll 1, \varepsilon) \equiv \omega_{sx}(h_1, \varepsilon)$ takes the asymptotic form

$$\omega_{sx}(h_1, \varepsilon) = \frac{\pi \omega_0(\varepsilon)}{\ln\left(\frac{32\varepsilon}{|h_1|}\right)}, \quad \omega_{sx}(h_1, \varepsilon) \to 0 \quad \text{as} \quad |h_1| \to 0. \tag{4.45}$$

In the rotation regime, for h_1 large enough $2\omega_p(h_1, \varepsilon) \approx \sqrt{2h_1} \approx I_1$. Figure 4.6 shows the dependence of ω_p on h_1, for $\varepsilon = 0.15$.

The resonance $\omega_1 = 0$ has a half-width $(\Delta I_1)^r = 2\sqrt{\varepsilon}$ in action space, so the variation of I_1 is bounded by $|\Delta I_1| \le 2\sqrt{\varepsilon}$ while I_2 remains constant. Therefore in (I_1, I_2) plane, $\omega_1 \to \omega_{sx}(h_1, \varepsilon) \to 0$ when $I_1 \to 2\sqrt{\varepsilon}$.

For $\varepsilon \neq 0, \mu \neq 0$ the original system (4.41) can be written as

$$\begin{aligned} H(I_1, I_2, \theta_1, \theta_2, t; \varepsilon, \mu) &= H_0(I_1, I_2, \theta_1; \varepsilon) + \mu V(\theta_1, \theta_2, t; \varepsilon), \\ \mu V(\theta_1, \theta_2, t; \varepsilon) &= \varepsilon\mu(\sin\theta_2 + \cos t)(\cos\theta_1 - 1), \end{aligned} \tag{4.46}$$

where H_0 is given by (4.43) and $\theta_2(t) = \omega_2 t + \theta_2^0$. Therefore the full Hamiltonian is a simple pendulum and a free rotator coupled by $V(\theta_1, \theta_2, t; \varepsilon)$.

Since the perturbation depends on θ_2 and t, it affects the phase oscillations at the resonance $\omega_1 = 0$ and leads to the formation of the stochastic layer around its separatrix. Moreover, due to the dependence of V on θ_2, the perturbation changes not only I_1 but I_2 as well, and then motion along the stochastic layer should proceed. Due to the stochasticity of the motion inside the layer, the variation of I_2 should be

[5]The whiskered torus is a generalization of a saddle equilibrium point and it is defined as the connected intersection of the stable and unstable manifolds or, in Arnold language, arriving and departing whiskers, W^- and W^+ respectively (see [1, 24] for further details).

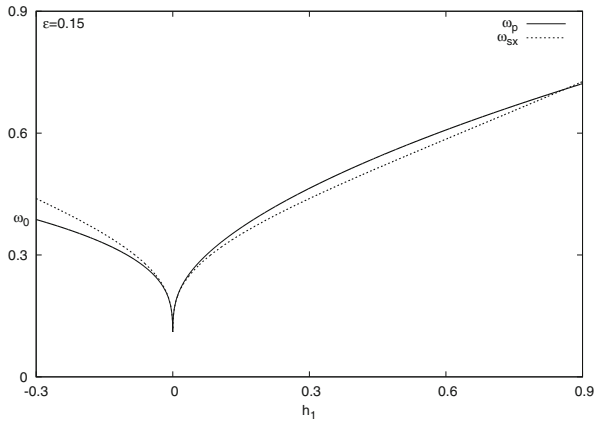

Fig. 4.6 Frequency of the pendulum H_1 given by (4.44), ω_p, and the approximation (4.45), ω_{sx}, for $\varepsilon = 0.15$. The separatrix corresponds to $h_1 = 0$ and the small oscillation frequency, $\omega_0 = \sqrt{\varepsilon} \approx 0.39$. Within the oscillation domain $h_1 \leq 0$ and $\omega(h_1) \leq \omega_0$, while for h_1 large enough, $2\omega \approx \sqrt{2h_1}$

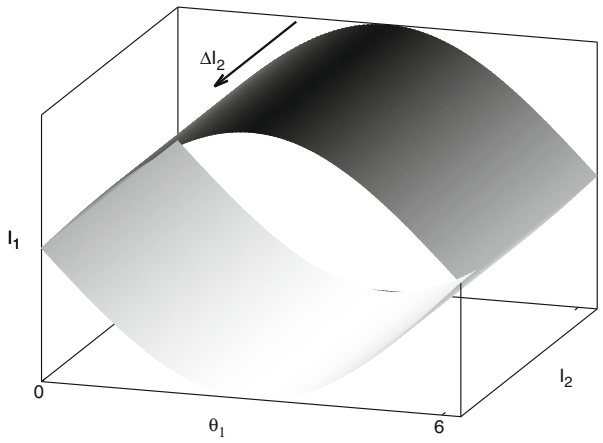

Fig. 4.7 Sketch of diffusion along I_2. The *arrow* indicates that ΔI_2 lies on the stochastic layer of the resonance $\omega_1 = 0$

also stochastic, giving rise to diffusion in I_2, as sketched in Fig. 4.7. In consequence, as I_2 would change unboundedly, a gross instability could set up. This is the way in which Arnold diffusion is described in an heuristic way in [8]. However, in this model, since the perturbation V vanishes at $I_1 = 0, \theta_1 = 0$, it is possible to build up a *transition chain* [1, 24] such that if ω_2 is irrational, then all tori defined by

$I_1 = 0, I_2 = \omega_2 > 0$ are *transition tori*,[6] and when $t \to \infty$, $|I_2(t) - I_2(0)| = \mathcal{O}(1)$, independently of ε and also of μ. Therefore a "large variation" of I_2 could take place. Let us state that by "large variation" we mean that I_2 could vary over a finite domain, which does not imply that it can be proved that I_2 changes without any bound. In fact, this is an open subject of research from a theoretical point of view. Therefore, any demonstration that diffusion might spread along the *resonance web* is quite far to be obtained, as pointed out in [46] and [9].

In the full Hamiltonian (4.46) however, $\omega_1 = 0$ is just one of the six first order resonances. Indeed, multiplying the different harmonics and using trigonometric relationships in $\mu V(\theta_1, \theta_2, t; \varepsilon)$ we obtain the following primary resonances at order ε and $\varepsilon\mu$:

$$\omega_1 = 0, \quad \omega_2 = 0, \quad \omega_1 \pm \omega_2 = 0 \quad \omega_1 \pm 1 = 0, \tag{4.47}$$

which are depicted in Fig. 4.8 in frequency space, illustrating their respective widths. In (4.47) but in the action or energy space, we should use either the approximations

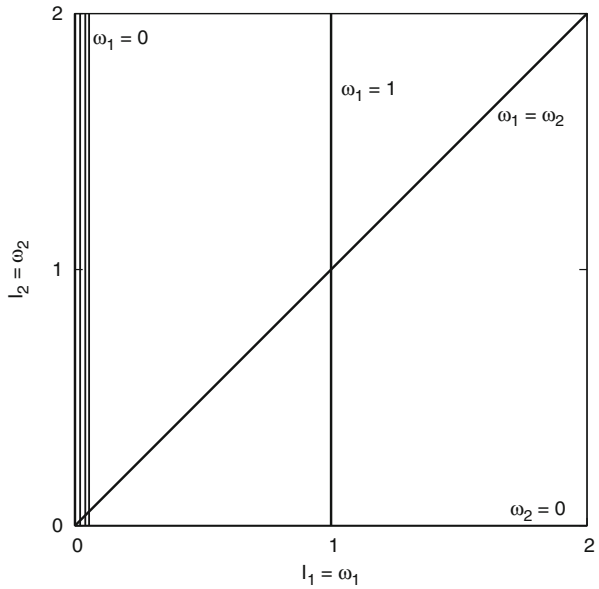

Fig. 4.8 Primary resonances in Arnold model (4.46) in the domain $I_1, I_2 \geq 0$ and considering $(\omega_1, \omega_2) = (I_1, I_2)$. The resonance $\omega_1 = 0$ has an amplitude $V_{10} = \varepsilon$ while for the rest, $V_{mn} = \varepsilon\mu \ll V_{10}$

[6]Roughly, a transition torus is a whiskered torus satisfying that points belonging to its arriving whisker W^-, intersect any manifold which is transverse to its departing whisker W^+. Therefore a transition chain is a set of k transition tori satisfying that W_l^+ of the l-transition torus intersects transversally W_{l+1}^- of the $(l+1)$-transition torus.

$\omega_1 \approx I_1$ in case $I_1 \gg 2\sqrt{\varepsilon}$, while $\omega_1 = \omega_p(h_1, \varepsilon)$ for $I_1 < 2\sqrt{\varepsilon}$ ($h_1 < 0$) or $\omega_1 = 2\omega_p(h_1, \varepsilon)$ in case $I_1 \gtrsim 2\sqrt{\varepsilon}$ ($h_1 > 0$).

For $I_1 \gg 2\sqrt{\varepsilon}$ the resonance "lines" intersect at seven fixed different points namely, $(I_1, I_2) = (0, 0), (0, \pm 1), (\pm 1, \pm 1)$.[7] Hence, as pointed out by Chirikov [8], the diffusion would spread over all this resonance set. Notice however, that for $\varepsilon\mu \ll \varepsilon \ll 1$ the diffusion rate should be negligible along all resonances except for $\omega_1 = 0$, since this resonance is the one that has the main strength, its amplitude being ε, while all the remaining resonances have amplitudes $\varepsilon\mu \ll \varepsilon$. Indeed, it can be shown (see for instance [8] and [9]) that the diffusion rate depends exponentially on $-1/\sqrt{V_{mn}}$, where V_{mn} stands for the amplitude of the above considered resonances.

Considering the fully perturbed motion, besides the ones given in (4.47), the full set of resonances is an integer linear combination of the form

$$m_1\omega_1 + m_2\omega_2 + m_3 = 0, \qquad m_1, m_2, m_3 \in \mathbb{Z}, \tag{4.48}$$

where again, $\omega_1 \approx I_1$ or $\omega_p(h_1, \varepsilon)$ depending on the value of $I_1/2\sqrt{\varepsilon}$. Therefore, the true picture of the Arnold web in action space[8] should be much more complex than the one presented in Fig. 4.8, since in that case it is assumed that $\varepsilon \ll \varepsilon\mu \ll 1$ and away from the origin it holds that $I_1 \gg 2\sqrt{\varepsilon}$ so that $\omega_1 = 2\omega_p \sim I_1$. In this case we expect vertical resonances for $m_2 = 0$, horizontal ones for $m_1 = 0$ and an infinite but countable set of curves for $m_1, m_2 \neq 0$ (see below).

For the sake of illustration, we present first the result of a numerical experiment adopting $\varepsilon = 0.05$ and $\mu = 0.0001$, such that the condition $\varepsilon\mu \ll \varepsilon \ll 1$ is fulfilled. Figure 4.9 shows the actual resonances while plotting just the MEGNO values larger than 2.05 for 10^6 initial conditions in the I_1, I_2 space with $\theta_1 = \pi, \theta_2 = t = 0$ after a total motion time 10^4. This plot should be compared to Fig. 4.8 where the main resonances, $\omega_1 = 0, \omega_2 = 0, \omega_1 = \omega_2$, and $\omega_1 \approx 1$ are clearly distinguished.

The expected width of the main resonance $\omega_1 = 0$, $(\Delta I_1)^r \approx 0.45$ is fully consistent with the computed one, and regarding the rest of the resonances, their width should be rather small, close to 4×10^{-3}, and thus they show up approximately as a single curve. Some other resonances do not appear as lines, while the one at $\omega_1 = 1$ do not arise exactly at $I_1 = 1$. Indeed, if we take the resonance condition given by (4.48) for $m_2 \neq 0$, we can rewrite it using the right value for ω_1,

$$\omega_2 = -\frac{m_1}{m_2}\omega_p(h_1, \varepsilon) - \frac{m_3}{m_2}, \tag{4.49}$$

[7] Note that for $I_1 \sim 2\sqrt{\varepsilon}$, $\omega_1 = 2\omega_p(h_1, \varepsilon)$ and the resonances should not intersect in the same set of points, since for instance the resonance $\omega_1 = \omega_2$ leads to a curve in the (I_1, I_2) plane that changes with ε.

[8] The web of all resonances such as (4.48) for all $m_1, m_2, m_3 \in \mathbb{Z}$.

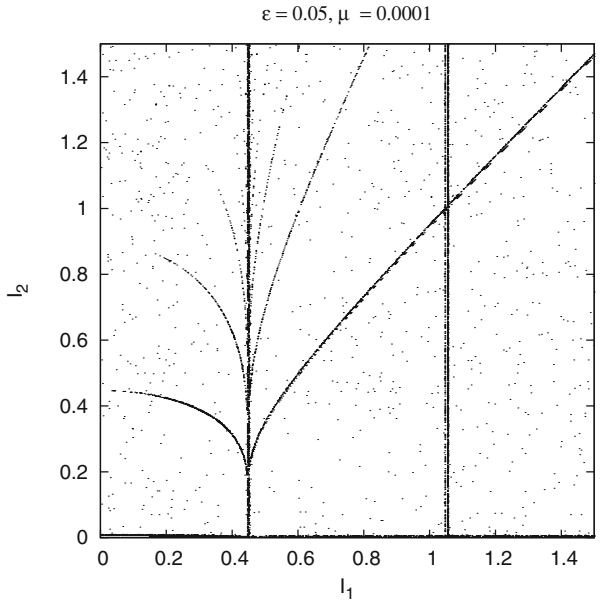

Fig. 4.9 Actual resonances in the Arnold model according to a MEGNO mapping on the (I_1, I_2)-plane for $\theta_1 = \pi$, $\theta_2 = t = 0$ and $\varepsilon\mu \ll \mu \ll \epsilon$. Region in *black* corresponds to chaotic domains, while those in *white* correspond to periodic or quasiperiodic motion (see text)

and several of the observed curves follow the very same pattern of $\omega_p(h_1, \varepsilon)$ given in Fig. 4.6.[9] In order to compare both figures recall that in Fig. 4.9, $\theta_1 = \pi$ so h_1 and I_1 are simply related by $I_1^2 = 2h_1 + 4\varepsilon$.

Many other resonances are obtained by means of the MEGNO for two sets of larger values of ε and μ, the results being displayed in Fig. 4.10. These are somewhat closer to a more realistic case since in a generic Hamiltonian, it is not possible to reduce the "perturbation" in such a way that it becomes exponentially small with respect to the integrable part. The assumption $\varepsilon \gtrsim \mu$ represents a typical situation in a system involving an integrable Hamiltonian plus a perturbation, which in fact is an artificial separation in a real problem (see for instance [66]).

In Fig. 4.10 we use the (h_1, I_2)-plane to display the resonances just to simplify the comparison of the pattern shown by high order resonances with the plot in Fig. 4.6. Several resonances of the form (4.49) can be observed, namely those of very low order, like $\omega_1 = 0$ of width 2ε (measured in h_1) where the separatrix appears at $h_1 = 0$. Many other high order ones show up exhibiting a similar pattern as that of $\omega_p(h_1, \varepsilon)$. Close to the separatrix all resonances accumulate at $(h_1, I_1) = (0, 0)$ following the very same behavior as ω_p.

[9] See next page for the estimation of the right position in the (I_1, I_2)-plane of the $\omega_1 = 1$ resonance.

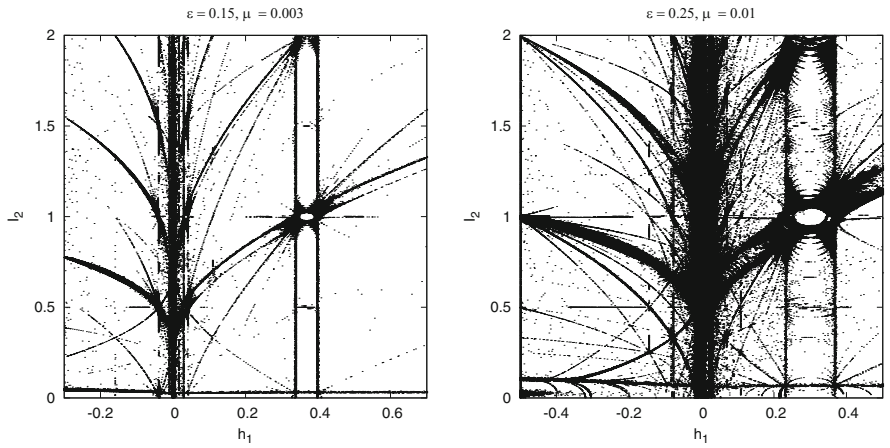

Fig. 4.10 True pictures through a MEGNO map on the (h_1, I_2)-plane for 10^6 initial values of (h_1, I_2) for a total motion time 10^4. *White* corresponds to regions of regular motion where $\overline{Y} < 2.05$, while those in *black* correspond to chaotic motion ($\overline{Y} \geq 2.05$). Section at $\theta_1 = \pi, \theta_2 = t = 0$ for $h_1 \geq -2\varepsilon, I_2 = \omega_2 > 0$

Let us take for instance the MEGNO's plot for $\varepsilon = 0.15$. The resonance $\omega_1 = 0$ should have a half-width $2\varepsilon = 0.3$, which is fully consistent with the computed one, and the separatrix appears at $h_1 = 0$ as expected. For the resonance $\omega_1 = 1$, the approximate value of $I_1^r = 1$ in fact corresponds to $h_1^r = 0.2$. However if we use the approximation (4.45) for the resonance condition $2\omega_p(h_1, \varepsilon) = 1$, it leads to $h_1^r \approx 0.4$ ($I_1^r \approx 1.2$) very close to the computed one. The obtained picture for $\varepsilon = 0.25$ shows a similar structure but, as expected, resonances are wider and many other high order resonances appear, particularly in the region close to the separatrix.

In both MEGNO contour plots the center of any resonance "channel" corresponds to 2D elliptic tori while the borders (the stochastic layer or homoclinic tangle) to 2D hyperbolic tori. At the intersection of two or more resonances a periodic orbit appears, which could be stable or unstable. In general, the intersection of two elliptic 2D tori leads to a stable periodic orbit and to a small domain of stable motion. From Fig. 4.10 we see that the MEGNO plots reveal the stability character of all the periodic orbits as well as a clear picture of the dynamics on the whole domain. However, from these plots nothing could be inferred concerning diffusion in action space, since as we have already pointed out, the MEGNO, as most chaos indicators, only provides information about the local dynamics of the Hamiltonian flow. Therefore we only have at hand just the behavior of the flow in any rather small open domain of every selected point in the grid. Nothing could be said about if it is possible that a chaotic orbit could explore a finite domain.

4.3.2 Models of Discrete Time

4.3.2.1 The Rational Shifted Standard Map

Let us consider the so-called Rational Shifted Standard Map (RSSM—see [13] for some additional details). This is a 2D area-preserving discrete dynamical system given by

$$y' = y + \varepsilon f(x), \qquad x' = x + \varepsilon y', \tag{4.50}$$

with $x \in [0, 2\pi)$, $y \in [0, 2\pi/\varepsilon)$, and where

$$f(x) = \frac{\sin(x+\varphi)}{1-\mu\cos x} - \Delta, \qquad \Delta = \frac{\mu \sin\varphi}{\sqrt{1-\mu^2}+1-\mu^2}. \tag{4.51}$$

Notice that (4.50) and (4.51) define some sort of Standard Map (SM) modified in order to have a no longer symmetric nor entire function f. Indeed, symmetry is lost through the introduction of the phase φ, while the insertion of the denominator, with the parameter $\mu \in [0, 1)$, breaks the entire character of f. The quantity Δ is fixed so that f has zero average, in order the RSSM be area-preserving.

After rescaling the y-variable by means of $y \to \varepsilon y$ such that both $x, y \in [0, 2\pi)$, the RSSM reads

$$y' = y + \varepsilon^2 f(x), \qquad x' = x + y', \tag{4.52}$$

and adopts an even closer form to that of the SM.

On expanding

$$\frac{1}{1-\mu\cos x} = 1 + \mu\cos x + \mu^2\cos^2 x + \mu^3\cos^3 x + \ldots, \tag{4.53}$$

and adopting $\varphi = 0$ in order to emphasize the comparison with the SM, after taking into account some trivial trigonometric identities, there results

$$f(x) = \frac{\sin x}{1-\mu\cos x} = \left(1+\frac{\mu^2}{4}\right)\sin x + \frac{\mu}{2}\sin 2x + \frac{\mu^2}{4}\sin 3x + \ldots. \tag{4.54}$$

To analyze the effect of changing φ, we perform the shift $x \to x + \varphi$ after which the equation for x in (4.52) remains invariant. On fixing $\varphi = \pi$

$$f(x) = \frac{\sin x}{1+\mu\cos x} = \left(1+\frac{\mu^2}{4}\right)\sin x - \frac{\mu}{2}\sin 2x + \frac{\mu^2}{4}\sin 3x + \ldots, \tag{4.55}$$

the map for $x, y \in [0, 2\pi)$ is seen to have a different dependence on the parameters than in the case in which $\varphi = 0$. Therefore a strong dependence of the dynamics on

φ is expected. Herein we will consider the two limiting values, $\varphi = 0, \pi$, in order to reduce the number of free parameters and to clearly show the differences with the SM.

Thus, from (4.54) and (4.55) it becomes clear that the RSSM shows up all the harmonics, instead of the solely term in $\sin x$ present in the SM. Furthermore, the resonances' width depends not only on ε^2, as it is the case in the SM, but on μ as well, and the resonance structure of both maps is similar when $\mu \to 0$. In the RSSM, for $\mu \neq 0$, all resonances (like $y/2\pi = 0, 1/3, 1/2, 2/3$) appear at order ε^2 and at different orders in μ, while in the SM, for instance the semi-integer resonance as $y = 1/2$ appears at ε^4 and those at $y = 1/3, 2/3$ show up at order ε^6, so as μ increases the resonances' interaction in the RSSM is stronger than in the SM.

The potential function for $f \equiv -V'$ is

$$V(x) = \pm\frac{1}{\mu}\ln\left\{1 - \mu\,\cos x\right\}, \qquad \mu \neq 0. \tag{4.56}$$

Expanding $V(x)$ in powers of μ and using the 2π-periodic δ in its Fourier form, the potential $U(x)$ of the corresponding Hamiltonian has the form

$$U(x) = \frac{\varepsilon^2}{4\pi^2}\left\{\left(1 + \frac{\mu^2}{4}\right)\sum_{n=-\infty}^{\infty}\cos(x + nt) + \right.$$
$$\left. + \frac{\mu}{4}\sum_{n=-\infty}^{\infty}\cos(2x + nt) + \frac{\mu^2}{12}\sum_{n=-\infty}^{\infty}\cos(3x + nt) + \ldots\right\}, \tag{4.57}$$

while the kinetic energy is given by $\hat{y}^2/2$, being $\hat{y} = y/2\pi$. Thus we can easily see how resonances appear at different orders in ε and μ.

The MEGNO has been applied to (4.52) in an equispaced grid of 1000×1000 pixels in the domain $(x/2\pi, y/2\pi) \in [0, 1)\times[0, 1)$, to obtain $\hat{Y}_{2,0}(N)$ for $N = 11{,}000$ (see (4.40) and discussion below). The results for $\varphi = 0$ and $\varphi = \pi$ are presented in Fig. 4.11, for $\varepsilon = 0.8$ and two different values of μ. There the pixels corresponding to initial conditions of regular behavior are plotted in white and those of chaotic behavior in black.[10] While for $\varphi = 0$ the regular regime prevails (plots on the left), the dynamics for $\varphi = \pi$ displays several chaotic domains (plots on the right) surrounding stochastic layers of resonances or as it seems, a connected chaotic open domain, but rotational invariant curves (joining the vertical boundaries) still exist. The variation of φ from 0 to π has a quite notorious effect on the dynamics as already mentioned in the theoretical discussion. The figures on the top corresponds to $\mu = 0.1$ while those on the bottom to $\mu = 0.2$. We can notice that increasing the value of μ changes the stability of the periodic orbit at $(0.5, 0.5)$ in the case

[10] We take slightly different threshold values in the figures just to display the global behavior, since for $\varphi = 0$ the map is mostly regular while for $\varphi = \pi$ it is strongly chaotic.

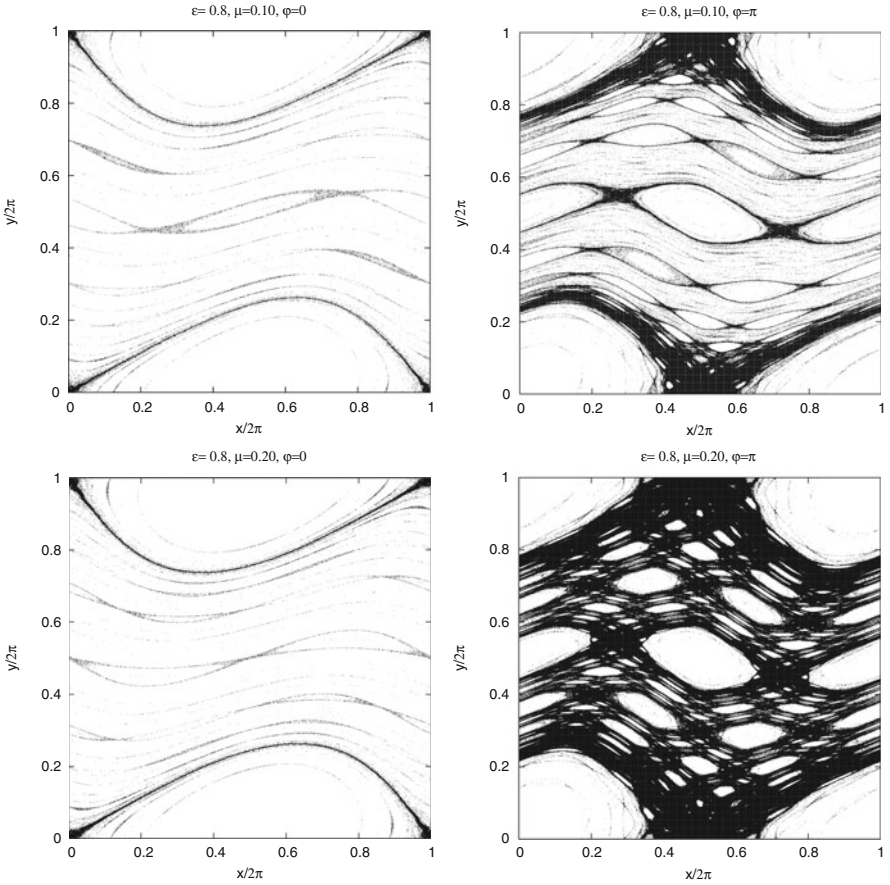

Fig. 4.11 $\hat{Y}_{2,0}$-levels for the RSSM corresponding to $\varepsilon = 0.8$, for $\varphi = 0$ (on the *left*) and $\varphi = \pi$ (on the *right*). The figures on the *top* correspond to $\mu = 0.1$ and those on the *bottom* to $\mu = 0.2$ Regions of regular behavior are depicted in *white* and those of chaotic behavior in *black*. The threshold values are 2×10^{-4} for $\varphi = 0$ and 2×10^{-2} for $\varphi = \pi$

of $\varphi = 0$. Meanwhile, for $\varphi = \pi$ the chaotic regime increases as larger values of μ are adopted. Notice that the MEGNO also succeeds in unveiling the high order resonance structure of this map.

4.3.2.2 The Coupled Rational Shifted Standard Map

Let us now turn to the Coupled Rational Shifted Standard Map (CRSSM), consisting of two coupled RSSM, defined by

$$\begin{aligned} y_1' &= y_1 + \varepsilon_1 f_1(x_1) + \gamma_+ f_3(x_1 + x_2) + \gamma_- f_3(x_1 - x_2), \\ y_2' &= y_2 + \varepsilon_2 f_2(x_2) + \gamma_+ f_3(x_1 + x_2) - \gamma_- f_3(x_1 - x_2), \end{aligned}$$

$$\begin{aligned} x_1' &= x_1 + \varepsilon_1 y_1', \\ x_2' &= x_2 + \varepsilon_2 y_2', \end{aligned} \tag{4.58}$$

with $x_i \in [0, 2\pi)$, $y_i \in [0, 2\pi/\varepsilon_i)$, $i = 1, 2$, and where

$$f_i(x) = \frac{\sin(x + \varphi_i)}{1 - \mu_i \cos x} - \Delta_i, \qquad \Delta_i = \frac{\mu_i \sin\varphi_i}{\sqrt{1 - \mu_i^2} + 1 - \mu_i^2}, \quad i = 1, 3, \tag{4.59}$$

with $\mu_i \in [0, 1)$ and again Δ_i fixed so that the f_i have zero average. Notice that two coupling terms in $(x_1 + x_2)$ and $(x_1 - x_2)$ have been added, γ_+ and γ_- being the coupling parameters. This map provides a more realistic representation of nonlinear resonance interactions than two coupled Standard Maps, so its dynamics would well serve as an improved simple model for many dynamical scenarios.

Again as in the RSSM, rescaling the y-variables, the CRSSM can be recast as

$$\begin{aligned} y_1' &= y_1 + \varepsilon_1^2 f_1(x_1) + \varepsilon_1\gamma_+ f_3(x_1 + x_2) + \varepsilon_1\gamma_- f_3(x_1 - x_2), \\ y_2' &= y_2 + \varepsilon_2^2 f_2(x_2) + \varepsilon_2\gamma_+ f_3(x_1 + x_2) - \varepsilon_2\gamma_- f_3(x_1 - x_2), \\ x_1' &= x_1 + y_1', \\ x_2' &= x_2 + y_2', \end{aligned} \tag{4.60}$$

where $(x_i, y_i) \in [0, 2\pi) \times [0, 2\pi)$.

The full set of primary resonances is determined by

$$k_1 y_1 + k_2 y_2 + 2\pi k_3 = 0, \qquad k_1, k_2, k_3 \in \mathbb{Z}. \tag{4.61}$$

Therefore, in the action plane, horizontal resonances correspond to the uncoupled (x_2, y_2) map and appear for $k_1 = 0$, the vertical ones correspond to the uncoupled (x_1, y_1) map obtained by setting $k_2 = 0$, while the coupling resonances given by $y_2 = -(k_1 y_1 + 2\pi k_3)/k_2$ are dense (but countable) in the (y_1, y_2)-space.

The MEGNO has been computed for an equispaced grid of 1000×1000 pixels in the domain $(y_1/2\pi, y_2/2\pi) \in [0, 1) \times [0, 1)$. The initial values for the remaining variables are $x_1 = 0, x_2 = 0$. The "right-stop" condition described in Sect. 4.2.4 has been applied so that for each initial condition the iteration is stopped after N iterates, with $10000 < N < 11000$, when the distance between the N-th iteration of the map and the initial condition is minimum.

A difference should be remarked with the action space of Arnold model discussed in the previous section. Indeed, by making the cross product $(x_1, y_1) \times (x_2, y_2)$ at $x_1 = x_2 = 0$, depending on the adopted value of φ and considering Fig. 4.11, we should expect that in the (y_1, y_2)-plane, only do the hyperbolic 2D tori (or to be precise, the homoclinic tangle) show up for $\varphi = 0$ while for $\varphi = \pi$, the picture should be similar to that of Fig. 4.10, since both, the elliptic and hyperbolic 2D tori would be present, as well as the nearly resonant 3D tori that are trapped in resonances.

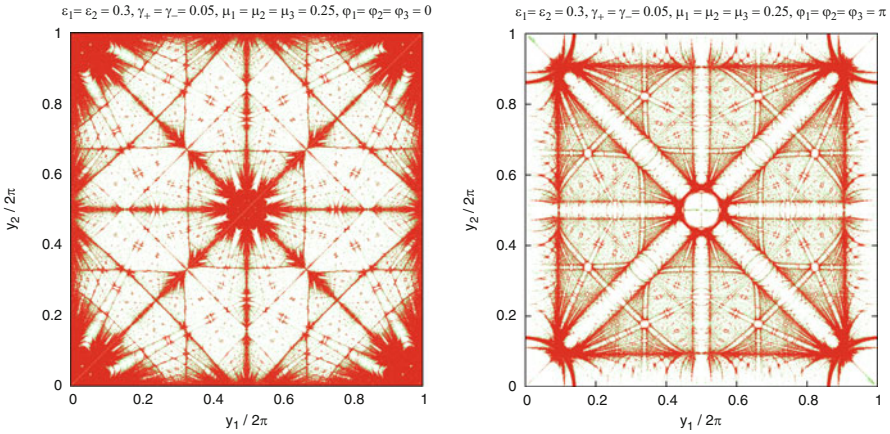

Fig. 4.12 $\hat{Y}_{2,0}$-levels for the CRSSM for different values of the parameters φ_i, 0 in the plot on the *left* and π in that on the *right*. The contour plots correspond to $\hat{Y}_{2,0}$ binned in three intervals; pixels corresponding to initial conditions of regular behavior are plotted in *white*, and those of chaotic behavior in *black* (*red*). With *gray* (*green*) we identify mild chaotic or even quasiperiodic motion

In order to illustrate the efficiency of the MEGNO to display the full dynamics of this 4D map, we show the results for $\Delta_i = 0$, i.e, $\varphi_i = 0$ and $\varphi_i = \pi$, $i = 1, 2, 3$, $\varepsilon_1 = \varepsilon_2 = 0.3$, $\mu_1 = \mu_2 = \mu_3 = 0.25$, and $\gamma_+ = \gamma_- = 0.05$, given in Fig. 4.12. The contour-like plots exhibit the obtained values for $\log(\hat{Y}_{2,0})$ given by (4.40) scaled in order to range from $-5 \le \log(\hat{Y}_{2,0}) < -3$, to $\log(\hat{Y}_{2,0}) \ge -3$. Recall that $\hat{Y}_{2,0} \to 0^-$ for quasiperiodic motion while $\hat{Y}_{2,0} > 0$ indicates chaotic dynamics. The initial conditions corresponding to regular orbits have been depicted in white, while those in black (red) are chaotic. The orbits holding intermediate values of $\hat{Y}_{2,0}$ are plotted in gray (green) and considered as, possibly, quasiperiodic or mildly chaotic.

Though the Arnold web could be obtained also by means of other chaos indicators, let us mention that since the MEGNO and its generalized version have a clear threshold value, both of them allow for separating regular and chaotic orbits, providing for the latter a measure of the mLCE. Therefore, instead of performing an automatic contour plot it is possible to select the MEGNO ranges to be depicted. This has several benefits when we are interested in separating regular motion and chaotic motion with different degrees of hyperbolicity.

The resonances defined by (4.61) can be clearly distinguished. The wider ones are the integer resonances of the uncoupled maps, however for $\varphi = 0$ almost all resonances have a rather small width due to the fact that in such a case we see only the hyperbolic part, except for a few high order resonances which show up as narrow "channels". The opposite picture corresponds to $\varphi = \pi$, where most resonances reveal their 2D elliptic and hyperbolic tori. Note that the periodic orbit at each resonance intersection is, as expected, unstable for $\varphi = 0$, while it is stable

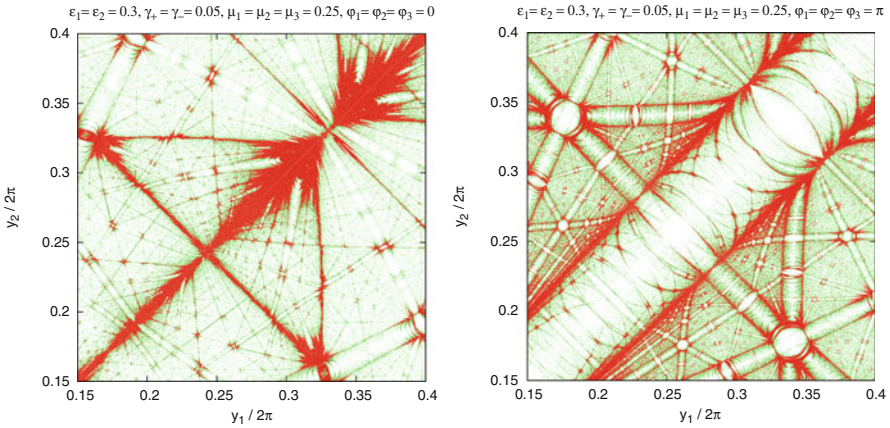

Fig. 4.13 Zoom of Fig. 4.12 in the domain $0.15 \leq y_1, y_2 \leq 0.4$

for $\varphi = \pi$. The complement of the set of 2D elliptic tori, 2D hyperbolic tori and periodic orbits, corresponds to 3D tori, where the motion is quasiperiodic.

In Fig. 4.13 we present a zoom of Fig. 4.12 corresponding to the region $0.15 \leq y_1, y_2 \leq 0.4$. In these $\hat{Y}_{2,0}$-contour plots we can distinguish many resonances of very high order as well as the dynamics in the resonance crossings. We can also notice how the stable and unstable manifolds bend to lead to either a regular or a chaotic domain. These manifolds are very important since they are the objects able to carry the motion arriving along one of the resonances either to the "other parts" of the resonance or to a different resonance. Besides, from the numerical results provided by the MEGNO, we could infer the true effect of the intersection of resonances of different order.

4.4 Comparison of Different Chaos Indicators

Some comparisons between particular indicators in the framework of specific studies were carried out, as those given for instance in [3, 47] and [37]. However, no systematic comparisons of the performance of several chaos indicators had been accomplished up to our comparative studies given in [48] and [49], which we briefly describe in the forthcoming subsections.

4.4.1 Comparative Studies for a Hamiltonian Flow

As already mentioned, the standard MEGNO has become a widespread technique for the study of Hamiltonian systems, particularly in the field of dynamical astronomy and astrodynamics, then, a comparison with other dynamical indicators

was in order. Therefore, in [49] a rather complex nonlinear system was addressed that reproduces many characteristics of real elliptical galaxies, namely, the self-consistent model introduced in [56]. Such a model was used as the scenario for a comprehensive comparison between the MEGNO and the mLCE, and even with the FLI. A detailed numerical and statistical study of a sample of orbits in the triaxial galactic system showed that the MEGNO is a suitable fast indicator to separate regular from chaotic motion and that it is particularly useful to investigate the nature of orbits that have a small but positive mLCE.

A rather good correlation was obtained between the MEGNO and the mLCE values for short, moderate and large integration times when considering just chaotic orbits, while the MEGNO provided much better results for regular motion. The FLI also looked like a reliable fast indicator, but since it has no reference value for regular motion, it might be useful to explore the phase space rather than to investigate the nature of a given orbit, unless of course the time evolution of such indicator was followed.

In [50] the same self-consistent triaxial stellar dynamical model was studied for different energy levels by means of some selected variational indicators and spectral analysis methods. Therein, the comparison of several variational indicators on different scenarios was addressed. Indeed, the Average Power Law Exponent (APLE) [47] and the MEGNO's estimation of the mLCE by a least squares fit of its time evolution were compared. The spectral analysis method selected for that investigation was the Frequency Modified Fourier Transform (FMFT) [63], which is just a slight variation of the FMA. Besides, a comparative study of the APLE, the FLI, the Orthogonal Fast Lyapunov Indicator (OFLI) [16] and the estimation of the mLCE obtained from the MEGNO's slope yielded as a result that the latter could be an appropriate alternative to the MEGNO when studying large samples of initial conditions. In fact, it succeeded in separating the chaotic and the regular components and in identifying the different levels of hyperbolicity (or exponential rate of divergence of nearby orbits) as well. Further, it turned out to be more reliable than the FMFT while describing chaotic domains.

4.4.2 Comparative Studies for Maps

In [48] the efficiency of several variational indicators of chaos when applied to mappings was compared. We considered the mLCE, the MEGNO, the Smaller Alignment Index (SALI) [67], its generalized version, the Generalized Alignment Index (GALI) [69], the FLI [19], the Dynamical Spectra of stretching numbers (SSN) [71] and the corresponding Spectral Distance (D) and the Relative Lyapunov Indicator (RLI) [62], which is based on the evolution of the difference between two close orbits. As a result of several experiments presented therein concerning two different 4D mappings, namely, a variant of Froeschlé's symplectic mapping [14, 17, 67, 68] and a system comprising two coupled Standard Maps, it was shown that a package composed of the FLI and the RLI (when a global analysis of the phase

portrait is pursued) and of the MEGNO and the SALI (if the objective is the analysis of individual orbits) turned out to be the best choices to yield a good description of the dynamics of the systems under study.

4.5 Further Applications of the MEGNO

In recent years the MEGNO has been widely used mainly in the field of dynamics of multi-planet extrasolar systems to address stability and habitability studies as well as in the solar system, galactic dynamics, astrobiology and chemistry. Herein, we include some references that would serve as illustration of this issue. We refer the reader to the original papers for details regarding the concomitant physical problems.

For extrasolar dynamical studies see for instance [20, 26–32, 52, 55, 61]. For research concerning Solar System dynamics we refer for example to [22] and [37], where the MEGNO technique is applied to the investigation of the dynamics of Jovian irregular satellites, to [60] which is devoted to the resonant structure of Jupiter's Trojan asteroids, its long-term stability and diffusion or to [21] where the evection resonance is considered. Interesting results in astrobiology are obtained while studying the dynamical habitability of exoplanetary systems (see [15, 36, 54]). Further applications of the MEGNO can be found in the study of space debris motion as in [38, 39, 70] among others, and of the chaotic motion of geosynchronous satellites as in [6, 40, 41].

As far as galactic studies are concerned, we can refer for instance to [7, 51, 72].

The use of this chaos indicator in rigid-body motion can be found in [2], and in the realm of chemistry in the analysis of intramolecular dynamics [65], or while revisiting the problem of driven coupled Morse oscillators [64]. Finally, bifurcations and chaos in different scenarios are studied by means of the MEGNO for instance in [4, 23, 25, 59], among many others.

4.6 Discussion

In this review we have described a rather simple technique, the *Mean Exponential Growth factor of Nearby Orbits* (MEGNO), which succeeds in providing detailed indications on the dynamics of continuous dynamical systems and maps. The intrinsic connection of this technique with the FLI and the mLCE is also presented.

The MEGNO furnishes an efficient algorithm that allows not only to clearly identify regular and irregular motion as well as stable and unstable periodic orbits, but also to obtain a quite good estimate of the mLCE in comparatively very short evolution times, for both ordered and chaotic components of phase space. This is a particular feature of this indicator that is not shared with many other techniques. In fact, we could deem that the derivation of the mLCE by a least squares fit of the

time evolution of the MEGNO is an alternative algorithm to get the time-scale for exponential divergence of nearby orbits but in rather short times in comparison with the classical approach.

Thus, by the application of this single tool it is possible to grasp the dynamics of the system over the whole phase space, and this procedure is a first attempt to get dynamical information about the motion using the whole orbit.

Moreover, there exists profuse numerical evidence of the MEGNO being a fast indicator capable of unveiling the hyperbolic structure of the phase space, as well as yielding a clear picture of the resonance structure in any dimensional systems. Besides, the MEGNO is shown to provide the actual size of a resonance of very high order as well as to reveal its internal structure.

Let us mention that the application of this technique to many different dynamical systems along the literature shows that it could be useful to investigate stability domains in exoplanetary models, chemical dynamics, space debris as well as to discuss purely theoretical features like bifurcation analysis.

Finally, regarding which is the more suitable chaos detection tool (based on the evolution of the tangent vector) we claim from our experience and in view of the nowadays available computational resources that, it is just a matter of the gained expertise on the adopted technique. However, let us say that the MEGNO is the one with a theoretical threshold value that allows to clearly separate regular from chaotic motion as well as it provides an accurate estimate of the mLCE by means of a very simple algorithm.

Therefore, a combination of any such indicator together with an accurate spectral technique, like the FMA, would be the best option to display the full dynamics of nonlinear systems which in general present a divided phase space.

Acknowledgements We should state clear that also Prof. C. Simó worked very hard developing this technique. Further, we are grateful to him for his illuminating discussions, comments and suggestions that helped us to write this chapter in a comprehensive way and any mistake is nothing but our own responsibility.

We also deeply appreciate the recommendations of the two thoughtful reviewers of this effort that serve to improve the final version.

This work was supported by grants from CONICET, UNLP and *Instituto de Astrofísica de La Plata*.

References

1. Arnold, V.I.: Soviet Math. Dokl. **5**, 581–585 (1964)
2. Barrio, R., Blesa, F., Elipe, A.: J. Astronaut. Sci. **54**(3–4), 359–368 (2006)
3. Barrio, R., Borczyk, W., Breiter, S.: Chaos Solitons Fractals **40**, 1697–1714 (2009)
4. Barrio, R., Blesa, F., Serrano, S.: Int. J. Bifurcat. Chaos **20**(5), 1293–1319 (2010)
5. Benettin, G., Galgani, L., Giorgilli, A., Strelcyn, J.M.: Meccanica **15**(1) Part I: Theory, 9–20; Part II: Numerical applications, 21–30 (1980)
6. Breiter, S., Wytrzyszczak, I., Melendo, B.: Adv. Space Res. **35**(7), 1313–1317 (2006)
7. Breiter, S., Fouchard, M., Ratajczak, R.: Mon. Not. R. Astron. Soc. **383**(1), 200–208 (2008)

8. Chirikov, B.V.: Phys. Rep. **52**, 263–379 (1979)
9. Cincotta, P.M.: New Astron. Rev. **46**, 13–39 (2002)
10. Cincotta, P.M., Simó, C.: Celest. Mech. Dyn. Astron. **73**(1–4), 195–209 (1999)
11. Cincotta, P.M., Simó, C.: In: Gurzadyan, V.G., Ruffini, R. (eds.) The Chaotic Universe. Advanced Series in Astrophysics and Cosmology, vol. 10, pp. 247–258. World Scientific (2000). ISBN: 978-981-279-362-1
12. Cincotta, P.M., Simó, C.: Astron. Astrophys. Suppl. **147**, 205–228 (2000)
13. Cincotta, P.M., Giordano, C.M., Simó, C.: Physica D **182**, 11–178 (2003)
14. Contopoulos, G., Giorgilli, A.: Meccanica **23**, 19–28 (1988)
15. Dvorak, R., Pilat-Lohinger, E., Bois, E., Schwarz, R., Funk, B., Beichman, C., Danchi, W., et al.: Astrobiology **10**(1), 33–43 (2010)
16. Fouchard, M., Lega, E., Froeschlé, Ch., Froeschlé, Cl.: Celest. Mech. Dyn. Astron. **83**, 205–222 (2002)
17. Froeschlé, C.: Astron. Astrophys. **16**, 172–189 (1972)
18. Froeschlé, C., Lega, E.: Celest. Mech. Dyn. Astron. **78**, 167–195 (2000)
19. Froeschlé, C., Gonczi, R., Lega, E.: Planet. Space Sci. **45**, 881–886 (1997)
20. Frouard, J., Compére, A.: Icarus **220**(1), 149–161 (2012)
21. Frouard, J., Fouchard, M., Vienne, A.: Astron. Astrophys. **515**(7) (2010). doi: 10.1051/0004-6361/200913048
22. Frouard, J., Vienne, A., Fouchard, M.: Astron. Astrophys. **532** (2011). doi: 10.1051/0004-6361/201015873
23. Gelfreich, V., Simó, C., Vieiro, A.: Physica D **243**(1), 92–110 (2013)
24. Giorgilli, A.: In: Benest, D., Froeschlé, C. (eds.) Les Methodes Modernes de la Mecanique Celeste, pp. 249–284. Frontières (1990). ISBN: 2-8633209-2
25. Gonchenko, S.V., Simó, C., Vieiro, A.: Nonlinearity **26**(3), 621–678 (2013)
26. Goździewski, K., Migaszewski, C.: Mon. Not. R. Astron. Soc. Lett. **397**(1), L16–L20 (2009)
27. Goździewski, K., Konacki, M., Maciejewski, A.J.: Astrophys. J. Lett. **622**(2I), 1136–1148 (2005)
28. Goździewski, K., Konacki, M., Wolszczan, A.: Astrophys. J. Lett. **619**(2I), 1084–1097 (2005)
29. Goździewski, K., Breiter, S., Borczyk, W.: Mon. Not. R. Astron. Soc. **383**(3), 989–999 (2006)
30. Goździewski, K., Konacki, M., Maciejewski, A.J.: Astrophys. J. Lett. **645**(1I), 688–703 (2006)
31. Goździewski, K., Migaszewski, C., Musielinski, A.: In: Proceedings of the International Astronomical Union 3, Symposium 249, pp. 447–460 (2007)
32. Goździewski, K., Slonina, M., Migaszewski, C., Rozenkiewicz, A.: Mon. Not. R. Astron. Soc. **430**(1), 533–545 (2013)
33. Guzzo, M., Lega, E., Froeschlé, C.: Physica D **163**, 1–25 (2002)
34. Hairer, E., Nørsett, S., Wanner, G.: Solving Ordinary Differential Equations I: Nonstiff Problems. Springer, New York (1987)
35. Hénon, M., Heiles, C.: Astron. J. **69**, 73 (1964)
36. Hinse, T.C., Michelsen, R., Jorgensen, U.G., Goździewski, K., Mikkola, S.: Astron. Astrophys. **488**(3), 1133–1147 (2008)
37. Hinse, T.C., Christou, A.A., Alvarellos, J.L.A., Goździewski, K.: Mon. Not. R. Astron. Soc. **404**(2), 837–857 (2010)
38. Hubaux, C., Lemâitre, A., Delsate, N., Carletti, T.: Adv. Space Res. **49**(10), 1472–1486 (2012)
39. Hubaux, Ch., Libert, A.S., Delsate, N., Carletti, T.: Adv. Space Res. **51**(1), 25–38 (2013)
40. Kuznetsov, E.D., Kaiser, G.T.: Cosmic Res. **45**(4), 359–367 (2007)
41. Kuznetsov, E.D., Kudryavtsev, A.O.: Russ. Phys. J. **52**(8), 841–849 (2009)
42. Laskar, J.: Icarus **88**, 266–291 (1990)
43. Laskar, J.: Physica D **67**, 257–281 (1993)
44. Laskar, J.: Astron. Astrophys. **287**(1), L9–L12 (1994)
45. Laskar, J., Froeschlé, C., Celletti, A.: Physica D **56**(2–3), 253–269 (1992)
46. Lochak, P.: In: Simó, C. (ed.) Hamiltonian Systems with Three or More Degrees of Freedom. NATO ASI Series, pp. 168–183. Kluwer Academic Publishers, The Netherlands (1999)
47. Lukes-Gerakopoulos, G., Voglis, N., Efthymiopoulos, C.: Physica A **387**, 1907–1925 (2008)

48. Maffione, N.P., Giordano, C.M., Cincotta, P.M.: Celest. Mech. Dyn. Astron. **111**, 285–307 (2011)
49. Maffione, N.P., Giordano, C.M., Cincotta, P.M.: Int. J. Non Linear Mech. **46**, 23–34 (2011)
50. Maffione, N.P., Darriba, L.A., Cincotta, P.M., Giordano, C.M.: Mon. Not. R. Astron. Soc. **429**(3), 2700–2717 (2013)
51. Manos, T., Bountis, T., Skokos, C.: J. Phys. A Math. Theor. **46**(25), 254017 (2013)
52. Martí, J.G., Giuppone, C.A., Beaugé, C.: Mon. Not. R. Astron. Soc. **433**(2), 928–934 (2013)
53. Mestre, M., Cincotta, P.M., Giordano, C.M.: Mon. Not. R. Astron. Soc. Lett. **404**, L100–L103 (2011)
54. Migaszewski, C., Goździewski, K., Hinse, T.C.: Mon. Not. R. Astron. Soc. **395**(3), 1204–1212 (2008)
55. Migaszewski, C., Slonina, M., Goździewski, K.: Mon. Not. R. Astron. Soc. **427**(1), 770–789 (2012)
56. Muzzio, J.C., Carpintero, D.D., Wachlin, F.C.: Celest. Mech. Dyn. Astron. **91**(1–2), 173 (2005)
57. Núñez, J.A., Cincotta, P.M., Wachlin, F.C.: Celest. Mech. Dyn. Astron. **54**(1–2), 43–53 (1996)
58. Prince, P., Dormand, J.: J. Comput. Appl. Math. **35**, 67 (1981)
59. Puig, J., Simó, C.: Regul. Chaotic Dyn. **16**(1), 61–78 (2011)
60. Robutel, P., Gabern, F.: Mon. Not. R. Astron. Soc. **372**(4), 1463–1482 (2006)
61. Saito, M.M., Tanikawa, K., Orlov, V.V.: Celest. Mech. Dyn. Astron. **116**(1), 1–10 (2013)
62. Sándor, Z., Érdi, B., Efthymiopoulos, C.: Celest. Mech. Dyn. Astron. **78**, 113–123 (2000)
63. Sidlichovský, M., Nesvorný, D.: Celest. Mech. Dyn. Astron. **65**, 137–148 (1997)
64. Sethi, A., Keshavamurthy, S.: Mol. Phys. **110**(9–10), 717–727 (2012)
65. Shchekinova, E., Chandre, C., Lan, Y., Uzer, T.: J. Chem. Phys. **121**(8), 3471–3477 (2004)
66. Simó, C.: In: Broer, H.W., Krauskopf, B., Vegter, G. (eds.) Global Analysis of Dynamical Systems, pp. 373–390. IOP Publishing, Bristol (2001)
67. Skokos, Ch.: J. Phys. A Math. Gen. **34**, 10029–10043 (2001)
68. Skokos, Ch., Contopoulos, G., Polymilis, C.: Celest. Mech. Dyn. Astron. **65**, 223–251 (1997)
69. Skokos, Ch., Bountis, T., Antonopoulus, Ch.: Physica D **231**, 30–54 (2007)
70. Valk, S., Delsate, N., Lemaitre, A., Carletti, T.: Adv. Space Res. **43**(10), 1509–1526 (2009)
71. Voglis, N., Contopoulos, G., Efthymiopoulos, C.: Celest. Mech. Dyn. Astron. **73**, 211–220 (1999)
72. Zorzi, A.F., Muzzio, J.C.: Mon. Not. R. Astron. Soc. **423**(2), 1955–1963 (2012)